nature communications

Article

https://doi.org/10.1038/s41467-024-54803-z

The capicua-ataxin-1-like complex regulates Notch-driven marginal zone B cell development and sepsis progression

Received: 7 May 2024

Accepted: 19 November 2024

Published online: 04 December 2024

Check for updates

Jong Seok Park[1], Minjung Kang[1], Han Bit Kim[1], Hyebeen Hong[1], Jongeun Lee[1], Youngkwon Song[1], Yunjung Hur[1], Soeun Kim[1], Tae-Kyung Kim[1] & Yoontae Lee[1,2]

Follicular B (FOB) and marginal zone B (MZB) cells are pivotal in humoral immune responses against pathogenic infections. MZB cells can exacerbate endotoxic shock via interleukin-6 secretion. Here we show that the transcriptional repressor capicua (CIC) and its binding partner, ataxin-1-like (ATXN1L), play important roles in FOB and MZB cell development. CIC deficiency reduces the size of both FOB and MZB cell populations, whereas ATXN1L deficiency specifically affects MZB cells. B cell receptor signaling is impaired only in *Cic*-deficient FOB cells, whereas Notch signaling is disrupted in both *Cic*-deficient and *Atxn1l*-deficient MZB cells. Mechanistically, ETV4 derepression leads to inhibition of *Notch1* and *Notch2* transcription, thereby inhibiting MZB cell development in B cell-specific *Cic*-deficient (*Cic$^{f/f}$;Cd19-Cre*) and *Atxn1l*-deficient (*Atxn1l$^{f/f}$;Cd19-Cre*) mice. In *Cic$^{f/f}$;Cd19-Cre and Atxn1l$^{f/f}$;Cd19-Cre* mice, humoral immune responses and lipopolysaccharide-induced sepsis progression are attenuated but are restored upon *Etv4*-deletion. These findings highlight the importance of the CIC-ATXN1L complex in MZB cell development and may provide proof of principle for therapeutic targeting in sepsis.

B cells are classified as B-1 or B-2 cells depending on their developmental origin[1]. B-1 cells, which mediate innate-like immunity by secreting natural antibodies, develop primarily in the fetal liver and are found in the pleural and peritoneal cavities[1]. Murine B-1 ($IgM^{hi}IgD^{lo}B220^{lo}CD19^{+}$ $CD23^{-}CD43^{+}$) cells are subdivided into B-1a ($CD5^{+}$) and B-1b ($CD5^{-}$) cells, depending on the CD5 expression on their surface[2]. B-2 cell development begins in the bone marrow. Pre-pro B cells derived from bone marrow hematopoietic stem cells acquire characteristic B cell surface markers, such as CD19 and B220, respond to cytokine signaling from molecules such as CXCL12, interleukin (IL)−7, and RANKL, and ultimately develop into immature B cells that express both immunoglobulin (Ig)M and IgD[3]. Immature B cells migrate to the spleen and differentiate into two distinct mature B cell types: one pathway leads to the production of follicular B (FOB, $CD19^{+}CD93^{-}CD21^{int}CD23^{+}$) cells via transitional type 1 B (T1B, $CD19^{+}CD93^{+}B220^{+}CD21^{lo}CD23^{-}IgM^{+}$) and T2B ($CD19^{+}CD93^{+}B220^{+}CD21^{lo}CD23^{+}IgM^{+}$) cells, whereas the other pathway leads to the generation of marginal zone B (MZB, $CD19^{+}CD93^{-}CD21^{high}CD23^{lo}$) cells via MZ progenitor (MZP, $CD19^{+}CD93^{+}CD21^{high}$) cells following T2B cell differentiation[4].

The final development into one of the two mature B cell types is determined by the balance among three signaling pathways: B cell receptor (BCR), B cell activating factor (BAFF), and Notch signaling[4]. A stronger BCR signal is necessary for differentiation into FOB cells, whereas a weaker BCR signal is sufficient for differentiation into MZB cells[4–6]. BAFF signaling is essential for the differentiation of immature B cells into both FOB and MZB cells, as well as the maintenance and survival of mature B cells[4,7,8]. Notch signaling is required for MZB cell

[1]Department of Life Sciences, Pohang University of Science and Technology (POSTECH), Pohang, Gyeongbuk, Republic of Korea. [2]Institute for Convergence Research and Education in Advanced Technology, Yonsei University, Seoul, Republic of Korea. e-mail: yoontael@postech.ac.kr

development[9,10]. Of the four mammalian Notch receptors, Notch1 and Notch2 are expressed in mature B cells[11,12]. When Notch receptors interact with stromal cells that express delta-like ligand 1 (DLL1), their extracellular and intracellular domains are sequentially cleaved by ADAM10 and γ-secretase, respectively[11]. The liberated Notch intracellular domain translocates to the nucleus, where it forms a transcriptional complex with transcription factors such as RBP-J and MAML[13]. This complex regulates the expression of target genes, including *Dtx1*, *Hes1*, *Cr2*, and *Asb2*[13–15].

FOB cells reside within the B cell follicle, whereas MZB cells are located in the MZ of the spleen, positioned between the white and red pulps[16]. Because of their distinct localization, FOB cells exhibit specificity in immune responses via interaction with T cells, whereas MZB cells are more likely to encounter blood-borne pathogens and primarily engage in T cell-independent (TI) immune responses[17]. In most cases, FOB cells differentiate into high-affinity antibody-producing plasma cells or memory B cells through the germinal center (GC) reaction[18]. MZB cells can also enter the GC and differentiate into plasma cells in response to lipid and polysaccharide pathogens circulating in the bloodstream[16,19–21]. MZB cells are involved in various diseases, such as pathogen infections and sepsis, through their involvement in cell-to-cell interactions and cytokine secretion[22–25].

Capicua (CIC) is an evolutionarily conserved transcriptional repressor that exists in two isoforms: CIC-S and CIC-L, of which CIC-L contains a unique amino-terminal region[26,27]. CIC directly binds to T(G/C)AATG(A/G)(A/G) sequences via its high mobility group box and C1 domain[28,29]. Representative CIC target genes include the *Pea3* group genes (*Etv1*, *Etv4*, and *Etv5*) and genes encoding negative regulators of the RAS-MAPK pathway, such as *Dusp4*, *Dusp6*, *Spry4*, *Spred1*, and *Spred2*[26]. CIC is stabilized by interacting with either ataxin-1 (ATXN1) or its paralog, ataxin-1-like (ATXN1L); ATXN1L plays a predominant role in stabilizing CIC compared with ATXN1[30,31]. CIC functions as a tumor suppressor in various cancer types[32–37]. CIC also plays a crucial role in the immune system via regulating thymic T cell development and the differentiation of follicular helper T cells and liver-resident memory-like CD8$^+$ T cells[38–42]. Additionally, CIC regulates B cell development. A CIC deficiency in B cells expands the B-1a cell population at the expense of B-2 cells[43,44]. This expansion in *Cic*-deficient mice is attributed to the upregulation of Bhlhe41, a key transcription factor for B-1a cell development, induced by the de-repression of Per2, a CIC target gene[43,45]. However, the regulatory mechanism of CIC influencing B-2 cell development, including that of FOB and MZB cells, remains unclear.

In this study, we examine the role of the CIC-ATXN1L complex in B-2 cell development. Our findings indicate that the CIC-ATXN1L complex regulates MZB cell development by modulating Notch signaling. In addition, we identify *Etv4* as a CIC target gene that inhibits Notch signaling and MZB cell development.

Results

ATXN1L deficiency suppresses MZB cell development

Our previous study has shown that the population of B-1a cells significantly expands in B cell-specific *Cic*-null (*Cic$^{f/f}$;Cd19-Cre*) mice, whereas those of FOB and MZB cells decrease[43] (Supplementary Fig. S1a, b). Didonna et al. showed that the B-1 cell frequency increased in the spleens of *Atxn1$^{-/-}$* mice, whereas that of MZB cells decreased[46], which was confirmed by our data (Supplementary Fig. S1c–f). However, the role of ATXN1L, a protein that stabilizes and interacts with CIC, in B cells remains unclear. To elucidate the role of ATXN1L in B cell development and function, we generated and characterized B cell-specific *Atxn1l*-null (*Atxn1l$^{f/f}$;Cd19-Cre*) mice. In contrast to *Cic$^{f/f}$;Cd19-Cre* and *Atxn1$^{-/-}$* mice (Supplementary Fig. S1a–c), the B-1 cell populations did not expand in the peritoneal cavities and spleens of *Atxn1l$^{f/f}$;Cd19-Cre* mice (Fig. 1a). In the spleens of *Atxn1l$^{f/f}$;Cd19-Cre* mice, the MZB and MZP cell populations were significantly reduced, whereas the T1B, T2B, and FOB cell formation remained normal (Fig. 1b–d). These results indicate that ATXN1L deficiency in B cells specifically impairs MZB cell development. Notably, we found that ATXN1L levels were higher in MZB cells than in FOB cells (Fig. 1e).

Humoral immune responses to antigens are attenuated in *Cic$^{f/f}$;Cd19-Cre* and *Atxn1l$^{f/f}$;Cd19-Cre* mice

MZB cells respond rapidly to TI antigens; however, they can also engage in a slower T cell-dependent (TD) immune response that is primarily mediated by FOB cells[16]. To investigate the effects of CIC or ATXN1L deficiency-induced alterations in B cell development on humoral immune responses, *Cd19-Cre* (control), *Cic$^{f/f}$;Cd19-Cre*, and *Atxn1l$^{f/f}$;Cd19-Cre* mice were immunized with the TI antigen NP-Ficoll and the TD antigen ovalbumin (OVA) via intravenous and intraperitoneal injections, respectively. Seven days after immunization, the mice were analyzed for serum NP-specific or OVA-specific IgM and IgG levels, as well as immune cell frequencies. Upon immunization with NP-Ficoll, the serum NP-specific IgM levels and Blimp1$^+$CD138$^+$ plasma cell populations were significantly decreased in both *Cic$^{f/f}$;Cd19-Cre* and *Atxn1l$^{f/f}$;Cd19-Cre* mice compared to control mice (Fig. 2a, b), suggesting that ttenuation of MZB cell development caused by the CIC and ATXN1L deficiency suppressed humoral immune responses to TI antigens. Upon immunization with OVA, both OVA-specific IgM and IgG levels were significantly reduced in *Atxn1l$^{f/f}$;Cd19-Cre* and *Cic$^{f/f}$;Cd19-Cre* mice (Fig. 2c). Consistent with these results, the populations of GCB and plasma cells were reduced in *Cic$^{f/f}$;Cd19-Cre* and *Atxn1l$^{f/f}$;Cd19-Cre* mice (Fig. 2d, e). The immune response to OVA was more robust in *Cic$^{f/f}$;Cd19-Cre* mice than that in *Atxn1l$^{f/f}$;Cd19-Cre* mice (Fig. 2c–e), potentially attributed to differences in B cell subset formation between *Cic$^{f/f}$;Cd19-Cre* and *Atxn1l$^{f/f}$;Cd19-Cre* mice.

Lipopolysaccharide (LPS)-induced sepsis progression is attenuated in *Cic$^{f/f}$;Cd19-Cre* and *Atxn1l$^{f/f}$;Cd19-Cre* mice

As MZB cells promote LPS-induced sepsis progression via IL-6 secretion induced by Toll-like receptor 4 signaling[22], we investigated sepsis progression in control, *Cic$^{f/f}$;Cd19-Cre*, and *Atxn1l$^{f/f}$;Cd19-Cre* mice following intravenous LPS injections. Most control mice died 72 h after the injection, whereas more than 50% *Cic$^{f/f}$;Cd19-Cre* mice survived (Fig. 3a). The serum IL-6 levels were significantly decreased in *Cic$^{f/f}$;Cd19-Cre* mice compared to those in control mice, whereas IL-10 levels were comparable between control and *Cic$^{f/f}$;Cd19-Cre* mice 12 h after LPS injection (Fig. 3b). Simultaneously, immune cell infiltration into the lung tissue was significantly reduced in *Cic$^{f/f}$;Cd19-Cre* mice compared to that in control mice (Fig. 3c). Similar results were observed in LPS-treated *Atxn1l$^{f/f}$;Cd19-Cre* mice (Fig. 3d–f). These data demonstrate that a CIC-ATXN1L complex deficiency in B cells attenuates the inflammatory response during endotoxic shock, thereby alleviating sepsis severity.

BCR signaling is attenuated in *Cic*-null FOB cells but not in *Atxn1l*-null FOB cells

We found that both FOB and MZB cell populations were reduced in *Cic$^{f/f}$;Cd19-Cre* mice, whereas only the MZB cell population was diminished in *Atxn1l$^{f/f}$;Cd19-Cre* mice. To examine the specific reduction in FOB cell populations of *Cic$^{f/f}$;Cd19-Cre* mice, we characterized T2B and FOB cells from control, *Cic$^{f/f}$;Cd19-Cre*, and *Atxn1l$^{f/f}$;Cd19-Cre* mice. Control and *Cic*-null T2B cells differentiated into FOB cells with similar efficiency upon anti-IgM treatment in vitro (Supplementary Fig. S2a). The apoptosis rate was comparable between control and *Cic*-null FOB cells in vitro (Supplementary Fig. S2b). The frequency of Ki-67$^+$ FOB cells was higher in *Cic$^{f/f}$;Cd19-Cre* and *Atxn1l$^{f/f}$;Cd19-Cre* mice than in control mice (Supplementary Fig. S2c, d). BAFF receptor signaling promotes B cell survival and T2B cell differentiation into FOB and MZB cells[4]; BAFF receptor levels were not reduced in *Cic*-null or *Atxn1l*-null T2B and FOB cells compared with those of their respective

https://doi.org/10.1038/s41467-024-54803-z

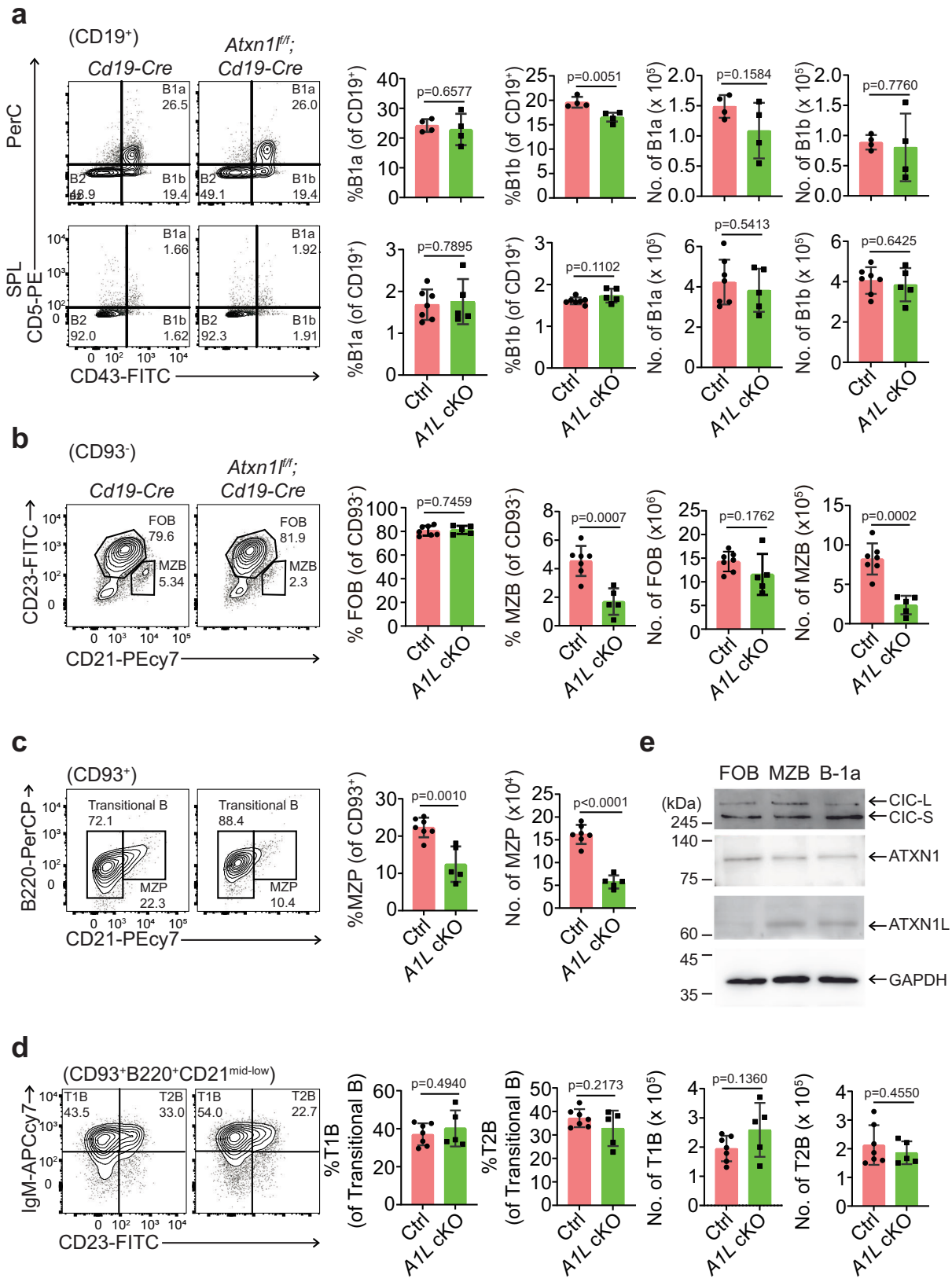

control cells (Supplementary Fig. S2e, f). These data demonstrate that the reduced FOB cell population in *Cic*$^{f/f}$*;Cd19-Cre* mice is not attributed to defects in T2B cell differentiation into FOB cells or in the survival and proliferation of FOB cells.

BCR signaling is crucial for peripheral B cell maintenance[47,48]; therefore, we examined the BCR signaling strength in FOB cells from control, *Cic*$^{f/f}$*;Cd19-Cre*, and *Atxn1l*$^{f/f}$*;Cd19-Cre* mice. Both tonic and anti-IgM-stimulated BCR signaling were significantly attenuated in *Cic*-null FOB cells compared with those in control cells (Fig. 4a). In contrast, these defects were rarely found in *Atxn1l*-null FOB cells (Fig. 4b). These results suggest that the attenuation of BCR signaling caused by CIC deficiency may decrease the FOB cell population.

https://doi.org/10.1038/s41467-024-54803-z

Fig. 1 | ATXN1L deficiency specifically reduces MZP and MZB cell populations. **a** Flow cytometry of B-1a ($CD19^+CD5^+CD43^+$) and B-1b ($CD19^+CD5^-CD43^+$) cells in the peritoneal cavities and spleens of *Cd19-Cre* and *Atxn1l$^{f/f}$;Cd19-Cre* mice. For peritoneal cavity analysis, $N = 5$ per both mice. For spleen analysis, $N = 7$ for *Cd19-Cre* and $N = 5$ for *Atxn1l$^{f/f}$;Cd19-Cre* mice. Flow cytometry of FOB and MZB cells (**b**), MZP cells (**c**), and T1B and T2B cells (**d**) in the spleens of *Cd19-Cre* and *Atxn1l$^{f/f}$;Cd19-Cre* mice. FOB ($CD19^+CD93^-CD21^{int}CD23^+$) and MZB ($CD19^+CD93^-CD21^{high}CD23^{lo}$) cells were initially gated as $CD93^-$ (AA4.1). T1B ($CD19^+CD93^+B220^+CD21^{lo}CD23^-IgM^+$), T2B ($CD19^+CD93^+B220^+CD21^{mid}CD23^+IgM^+$), and MZP ($CD19^+CD93^+CD21^{high}$) cells were gated as $CD93^+$ (AA4.1). $N = 7$ for *Cd19-Cre* and $N = 5$ for *Atxn1l$^{f/f}$;Cd19-Cre*. **e** Western blotting to detect the levels of CIC, ATXN1, and ATXN1L in FOB, MZB, and B-1a cells. FOB and MZB cells were prepared from the spleens of C57BL/6 mice, whereas B-1a cells were isolated from the peritoneal cavities of the same mice. Data represent 2–3 independent experiments. Statistics: two-tailed Student's *t*-test (**a**–**d**). Bar graphs present the data as mean ± S.D. Ctrl: *Cd19-Cre* and A1L cKO: *Atxn1l$^{f/f}$;Cd19-Cre*. MZP marginal zone progenitor cells, MZB marginal zone B cells, and FOB follicular B cells. Source data are provided as a Source Data file.

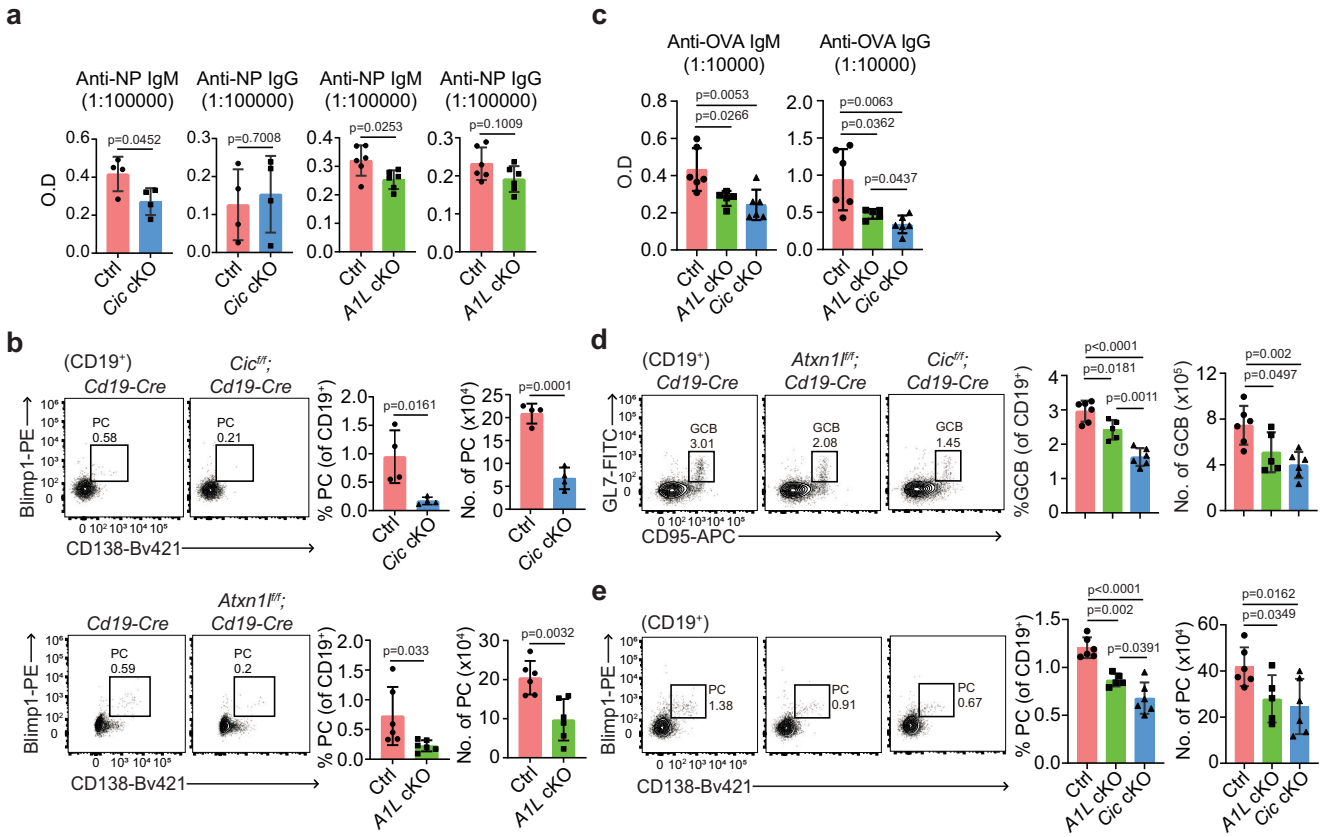

Fig. 2 | Humoral immune responses are attenuated in *Cic$^{f/f}$;Cd19-Cre* and *Atxn1l$^{f/f}$;Cd19-Cre* mice. **a**, **b** *Cd19-Cre*, *Cic$^{f/f}$;Cd19-Cre*, and *Atxn1l$^{f/f}$;Cd19-Cre* mice were immunized with NP-Ficoll for 7 days. **a** Serum NP-specific IgM and IgG levels determined using ELISA. **b** Flow cytometry of splenic plasma cells. $N = 4$ for *Cd19-Cre* and *Cic$^{f/f}$;Cd19-Cre* groups, and $N = 6$ for *Cd19-Cre* and *Atxn1l$^{f/f}$;Cd19-Cre* groups. **c**–**e** *Cd19-Cre*, *Cic$^{f/f}$;Cd19-Cre*, and *Atxn1l$^{f/f}$;Cd19-Cre* mice were immunized with OVA in alum for 7 days. **c** Serum OVA-specific IgM and IgG levels determined using ELISA. **d**, **e** Flow cytometry of splenic GCB cells ($CD19^+GL\text{-}7^+CD95^+$) (**d**) and plasma cells ($CD19^+CD138^+Blimp1^+$) (**e**). $N = 6$ for *Cd19-Cre* and *Cic$^{f/f}$;Cd19-Cre*, and $N = 5$ for *Atxn1l$^{f/f}$;Cd19-Cre*. Data represent two independent experiments. Statistics: two-tailed Student's *t*-test (**a**, **b**) and one-way ANOVA with Tukey's multiple comparisons test (**c**–**e**). Bar graphs present data as mean ± S.D. Ctrl: *Cd19-Cre*, Cic cKO: *Cic$^{f/f}$;Cd19-Cre*, and A1L cKO: *Atxn1l$^{f/f}$;Cd19-Cre*. ELISA enzyme-linked immunosorbent assay, OVA ovalbumin, and GCB germinal center B cells. Source data are provided as a Source Data file.

Notch signaling is downregulated because of the CIC-ATXN1L complex deficiency

To understand the mechanism underlying the CIC or ATXN1L deficiency inhibiting MZB cell development, we characterized MZB cells from control, *Cic$^{f/f}$;Cd19-Cre*, and *Atxn1l$^{f/f}$;Cd19-Cre* mice. Apoptosis rates were significantly reduced in *Cic*-null or *Atxn1l*-null MZB cells compared with those in control cells in vitro (Supplementary Fig. S2g, h). Similar to the results for FOB cells (Supplementary Fig. S2c, d), the frequencies of Ki-67$^+$ MZB cells were increased in *Cic$^{f/f}$;Cd19-Cre* and *Atxn1l$^{f/f}$;Cd19-Cre* mice compared with that in control mice (Supplementary Fig. S2i, j). BAFF receptor levels were higher in *Cic*-null and *Atxn1l*-null MZB cells than in control cells (Supplementary Fig. S2e, f). The phosphorylation of BLNK and BTK following BCR stimulation showed similar patterns in control, *Cic*-null, and *Atxn1l*-null MZB cells (Supplementary Fig. S2k, l). These data suggest that the reduced MZB cell population caused by the CIC and ATXN1L deficiency is not attributed to defects in cell proliferation, cell viability, or BCR signaling.

We then examined the gene expression profiles in control and *Cic*-null MZB cells using RNA sequencing. In total, 775 genes were differentially expressed in *Cic*-null MZB cells (505 upregulated and 270 downregulated; Supplementary Data 1) compared with the expression in control cells ($\log_2$ fold-change > 0.5 and $P < 0.01$). Several known CIC target genes, including *Etv4*, *Etv5*, *Spry4*, *Spred1*, and *Dusp4*, were among the upregulated genes in *Cic*-null MZB cells (Fig. 5a and Supplementary Data 1). Kyoto Encyclopedia of Genes and Genomes (KEGG) pathway and gene ontology (GO) analyses of differentially expressed genes (DEGs) in *Cic*-null MZB cells revealed that the Notch

https://doi.org/10.1038/s41467-024-54803-z

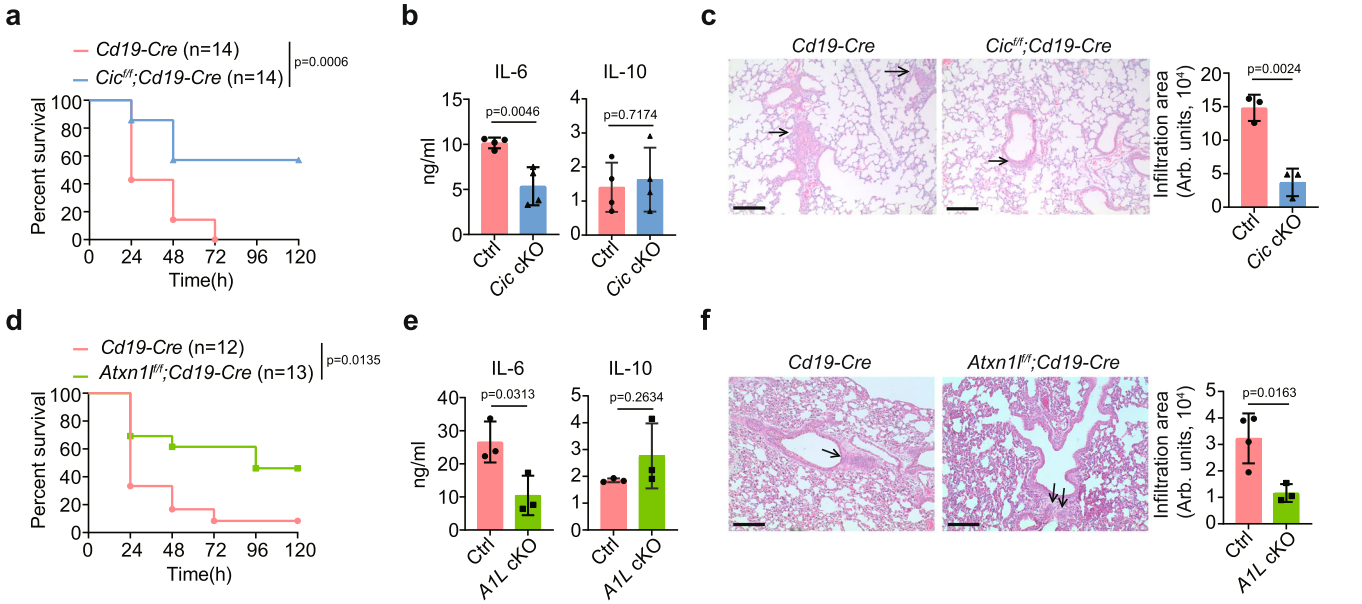

Fig. 3 | LPS-induced sepsis progression is attenuated in *Cic*$^{f/f}$*;Cd19-Cre* and *Atxn1l*$^{f/f}$*;Cd19-Cre* mice. a–**c** Female *Cd19-Cre* and *Cic*$^{f/f}$*;Cd19-Cre* mice were injected intravenously with LPS. Serum samples and lung tissues were collected from *Cd19-Cre* and *Cic*$^{f/f}$*;Cd19-Cre* mice 12 h after LPS injection. **a** Survival rate of LPS-treated mice. Mortality was monitored every 24 h. $N = 14$ per group. **b** Serum IL-6 and IL-10 levels determined using ELISA. $N = 4$ per group. **c** Histology of immune cell infiltration into lung tissue. Arrows indicate immune cell-infiltrated regions. $N = 3$ per group. Scale bar: 100 μm. **d**–**f** Female *Cd19-Cre* and *Atxn1l*$^{f/f}$*;Cd19-Cre* mice were injected intravenously with LPS. Serum samples and lung tissues were collected from *Cd19-Cre* and *Atxn1l*$^{f/f}$*;Cd19-Cre* mice 12 h after LPS injection. **d** Survival rate of LPS-treated mice. Mortality was monitored every 24 h. $N = 12$ for *Cd19-Cre* and $N = 13$ for *Atxn1l*$^{f/f}$*;Cd19-Cre*. **e** Serum IL-6 and IL-10 levels determined using ELISA. $N = 3$ per group. **f** Histology of immune cell infiltration into lung tissue. Arrows indicate immune cell-infiltrated regions. $N = 4$ for *Cd19-Cre* and $N = 3$ for *Atxn1l*$^{f/f}$*;Cd19-Cre*. Scale bar: 100 μm. Data represent 2–3 independent experiments. Statistics: Log-rank (Mantel-Cox) test (**a**, **d**) and two-tailed Student's *t*-test (**b**, **c**, **e**, **f**). Bar graphs present data as mean ± S.D. Ctrl: *Cd19-Cre*, Cic cKO: *Cic*$^{f/f}$*;Cd19-Cre*, and A1L cKO: *Atxn1l*$^{f/f}$*;Cd19-Cre*. LPS lipopolysaccharide, IL interleukin, and ELISA enzyme-linked immunosorbent assay. Source data are provided as a Source Data file.

signaling pathway was significantly downregulated in these cells (Supplementary Fig. S3 and Supplementary Data 2 and 3). Gene set enrichment analysis (GSEA) also showed that the Notch signaling-related genes were downregulated in *Cic*-null MZB cells (Fig. 5b). We validated the downregulation of genes involved in the Notch signaling pathway, including *Notch1*, *Notch2*, *Hes1*, *Dtx1*, *Asb2*, and *Cr2*, in *Cic*-null and *Atxn1l*-null MZB cells using real-time quantitative polymerase chain reaction (RT-qPCR; Fig. 5c, d). At the protein level, NOTCH1, NOTCH2, and CD21 (encoded by *Cr2*) expression was downregulated in *Cic*-null and *Atxn1l*-null MZP and MZB cells (Fig. 5e, f). To evaluate the differentiation potential of *Cic*-null and *Atxn1l*-null T1B cells into MZB cells, we co-cultured T1B cells with control or DLL1-expressing OP9 cells and assessed the efficiency of Notch signaling activation in promoting T1B cell differentiation into MZB cells in vitro. Both *Cic*-null and *Atxn1l*-null T1B cells were less efficient in differentiating into MZB cells compared with control cells (Fig. 5g, h). Additionally, *Atxn1* knockdown further reduced the efficiency of MZB cell differentiation in *Atxn1l*-null T1B cells (Fig. 5i), suggesting redundancy between ATXN1 and ATXN1L in the regulation of Notch signaling-induced MZB cell development. Overall, these results demonstrate that the CIC-ATXN1L complex promotes MZB cell development via activation of Notch signaling.

ETV4 is a CIC target gene that suppresses Notch signaling and MZB cell development

Next, we identified the CIC target genes that downregulate Notch signaling in *Cic*-null and *Atxn1l*-null MZB cells. Notch signaling is reported to be hyperactivated in the lacrimal gland epithelial cells of *Etv1*/*Etv4*/*Etv5* triple-knockout mice, accompanied by *Notch1*, *Notch2*, and *Notch3* overexpression[49]. Therefore, we hypothesized that the de-repression of *Etv4* and *Etv5* downregulated the *Notch1* and *Notch2* expression in *Cic*-null and *Atxn1l*-null MZB cells. The RT-qPCR analysis confirmed the significant upregulation of *Etv4* and *Etv5* expression in both *Cic*-null and *Atxn1l*-null MZB cells compared with the expression in control cells (Fig. 6a, b). To determine ETV4- and ETV5-induced regulation of *Notch1* and *Notch2* expression at the transcription level, we constructed luciferase reporters with either *Notch1* or *Notch2* promoter regions (upstream 1 kb from the transcription start site; Supplementary Fig. S4a, b). ETV4 *suppressed Notch1 and Notch2* promoter activity in HEK293T and HeLa cells, respectively (Supplementary Fig. S4c), but ETV5 did not (Supplementary Fig. S4d and e). ETV4 did not inhibit *Notch1* and *Notch2* promoter activity when the cell lines were switched (Supplementary Fig. S4f, g), suggesting a cell type-specific suppression of *Notch1* and *Notch2* expression by ETV4. We also identified ETV4 binding motifs (5′-GGAA-3′) that contributed to ETV4-mediated repression of *Notch1* and *Notch2* promoter activity. When the second ETV4 binding motif was mutated, ETV4 could no longer repress *Notch1* promoter activity (Supplementary Fig. S4a–c). Disruption of both ETV4 binding motifs almost completely abolished the inhibitory effect of ETV4 overexpression on *Notch2* promoter activity (Supplementary Fig. S4b, c). To determine whether ETV4 overexpression downregulates *Notch1* and *Notch2* expression in MZB cells, we infected these cells with a retrovirus expressing ETV4 and analyzed NOTCH1 and NOTCH2 expression using flow cytometry. MZB cells infected with the ETV4-expressing virus exhibited a reduced surface expression of both NOTCH1 and NOTCH2 (Fig. 6c). Additionally, we found that ETV4 binds to the promoter regions of *Notch1* and *Notch2*, which contain ETV4 binding motifs, in *Cic*-null B-2 cells (Fig. 6d and Supplementary Fig. S4a, b). These results demonstrate that ETV4 functions as a transcriptional repressor of *Notch1* and *Notch2* expression in MZB cells.

To determine the suppression of Notch signaling and MZB cell development via CIC or ATXN1L deficiency-meditated ETV4 de-

https://doi.org/10.1038/s41467-024-54803-z

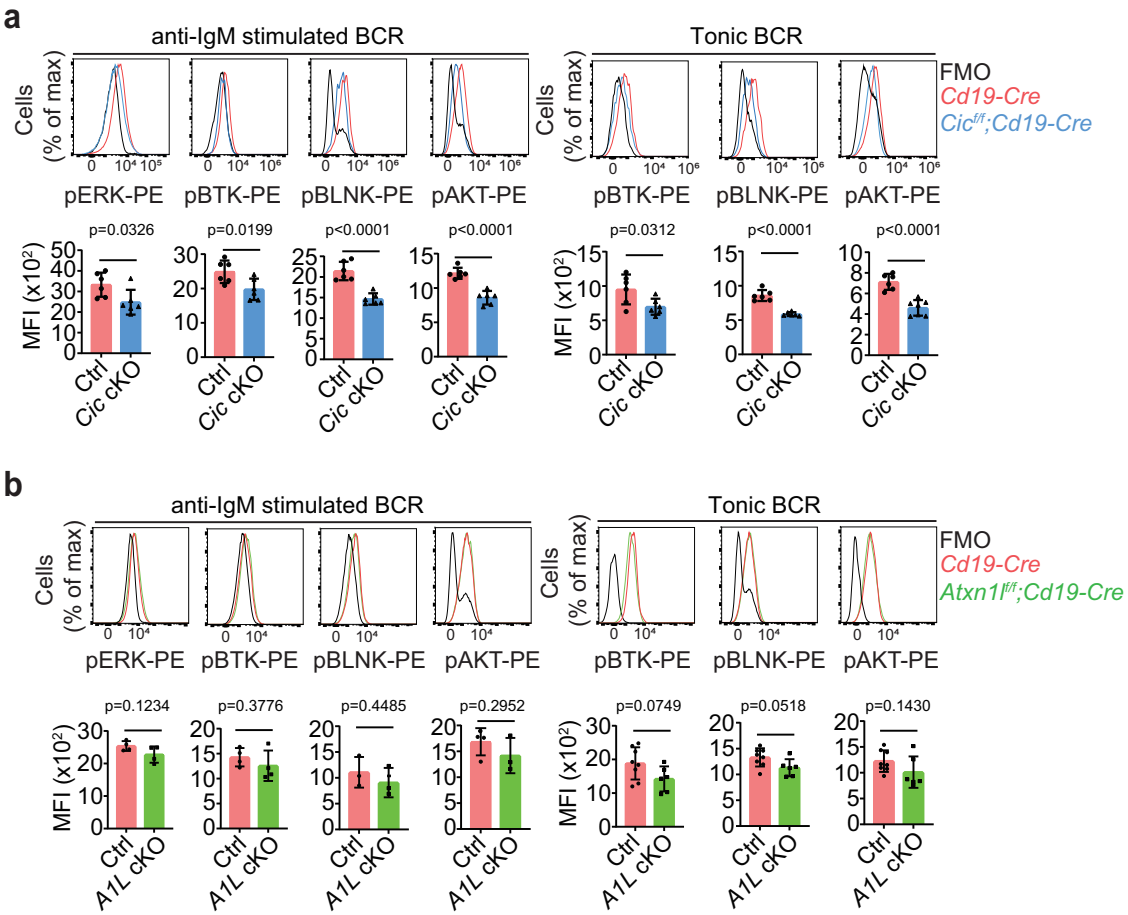

Fig. 4 | BCR signaling is attenuated in *Cic*-null FOB cells. Analysis of anti-IgM-stimulated and tonic BCR signaling in *Cic*-null (**a**) and *Atxn1l*-null (**b**) FOB cells. Phosphorylated-ERK (pERK), phosphorylated-BTK (pBTK), phosphorylated-BLNK (pBLNK), and phosphorylated-AKT (pAKT) levels were determined using flow cytometry and presented as MFI. For the BCR signaling analysis in control and *Cic*-null FOB cells, $N = 6$ per group (**a**). For the analysis of pERK and pBTK levels in control and *Atxn1l*-null FOB cells stimulated with anti-IgM, $N = 4$ per group (**b**). For the analysis of pBLNK levels in control and *Atxn1l*-null FOB cells stimulated with anti-IgM, $N = 3$ per group (**b**). For the analysis of pAKT levels in control and *Atxn1l*-null FOB cells stimulated with anti-IgM, $N = 4$ for *Cd19-Cre* and $N = 3$ for *Atxn1l$^{f/f}$;Cd19-Cre* (**b**). For the tonic BCR signaling analysis in control and *Atxn1l*-null FOB cells, $N = 8$ for *Cd19-Cre* and $N = 6$ for *Atxn1l$^{f/f}$;Cd19-Cre* (**b**). Data represent 2–3 independent experiments. Statistics: two-tailed Student's *t*-test (**a**, **b**). Bar graphs present data as mean ± S.D. Ctrl: *Cd19-Cre*, Cic cKO: *Cic$^{f/f}$;Cd19-Cre*, and A1L cKO: *Atxn1l$^{f/f}$;Cd19-Cre*. BCR B cell receptor, MFI mean fluorescence intensity, and FOB, follicular B cells. Source data are provided as a Source Data file.

repression, we generated *Etv4* and *Cic* (*Etv4$^{-/-}$;Cic$^{f/f}$;Cd19-Cre*) or *Atxn1l* (*Etv4$^{-/-}$;Atxn1l$^{f/f}$;Cd19-Cre*) double mutant mice. The MZB and MZP cell populations were restored to control mouse levels in *Etv4$^{-/-}$;Cic$^{f/f}$;Cd19-Cre* mice (Fig. 6e, f). In contrast, *Etv4* allele deletion did not rescue the FOB, GCB, and B-1a cell phenotypes in *Cic$^{f/f}$;Cd19-Cre* mice (Fig. 6e and Supplementary Fig. S5), indicating that the regulation of B-1a, MZB, and FOB cell development by CIC was mediated by differential molecular mechanisms[43]. The frequency of T2B cells was significantly restored in *Etv4$^{-/-}$;Cic$^{f/f}$;Cd19-Cre* mice (Fig. 6g). The MZB and MZP cell populations were also recovered in *Etv4$^{-/-}$;Atxn1l$^{f/f}$;Cd19-Cre* mice (Fig. 6h, i). Furthermore, ETV4 deficiency significantly restored NOTCH1, NOTCH2, and CD21 levels in *Cic*-null and *Atxn1l*-null MZB and MZP cells (Fig. 6j, k). Conversely, the loss of *Etv5* did not rescue the FOB, MZB, MZP, and T2B cell population decrease caused by CIC deficiency (Supplementary Fig. S6). Notably, the formation of FOB, MZP, and MZB cells and the expression of NOTCH1 and NOTCH2 in these subsets were comparable between wild-type (WT) and *Etv4$^{-/-}$* mice (Supplementary Fig. S7), indicating that ETV4 is not essential for the regulation of B cell development and Notch signaling under steady-state conditions. Collectively, these results indicate that ETV4 de-repression due to the CIC-ATXN1L complex deficiency suppresses *Notch1* and *Notch2* expression, consequently causing defects in MZB cell development.

The diminished IgM production and attenuated sepsis progression in *Cic$^{f/f}$;Cd19-Cre* mice are caused by defects in MZB cell development

The defects in MZB cell development in *Cic$^{f/f}$;Cd19-Cre* mice were specifically recovered via *Etv4* allele deletion; however, it remains unclear whether these defects are the cause for the attenuated humoral immune responses and sepsis progression in *Cic$^{f/f}$;Cd19-Cre* mice. For clarification, we analyzed the serum levels of NP-specific or OVA-specific IgM and IgG and the frequencies of immune cells in control, *Cic$^{f/f}$;Cd19-Cre*, and *Etv4$^{-/-}$;Cic$^{f/f}$;Cd19-Cre* mice immunized with NP-Ficoll or OVA. The decreased Blimp1^{+}CD138^{+} plasma cell populations and serum NP-specific IgM levels in *Cic$^{f/f}$;Cd19-Cre* mice immunized with NP-Ficoll were significantly restored by ETV4 deficiency (Fig. 7a, b), suggesting that the attenuated humoral immune response to TI antigens was caused by defects in MZB cell development in *Cic$^{f/f}$;Cd19-Cre* mice. Upon OVA immunization, *Etv4$^{-/-}$;Cic$^{f/f}$;Cd19-Cre* mice did not restore the GCB and plasma cell populations, and the serum anti-OVA IgG levels did not increase, in comparison with the observed

https://doi.org/10.1038/s41467-024-54803-z

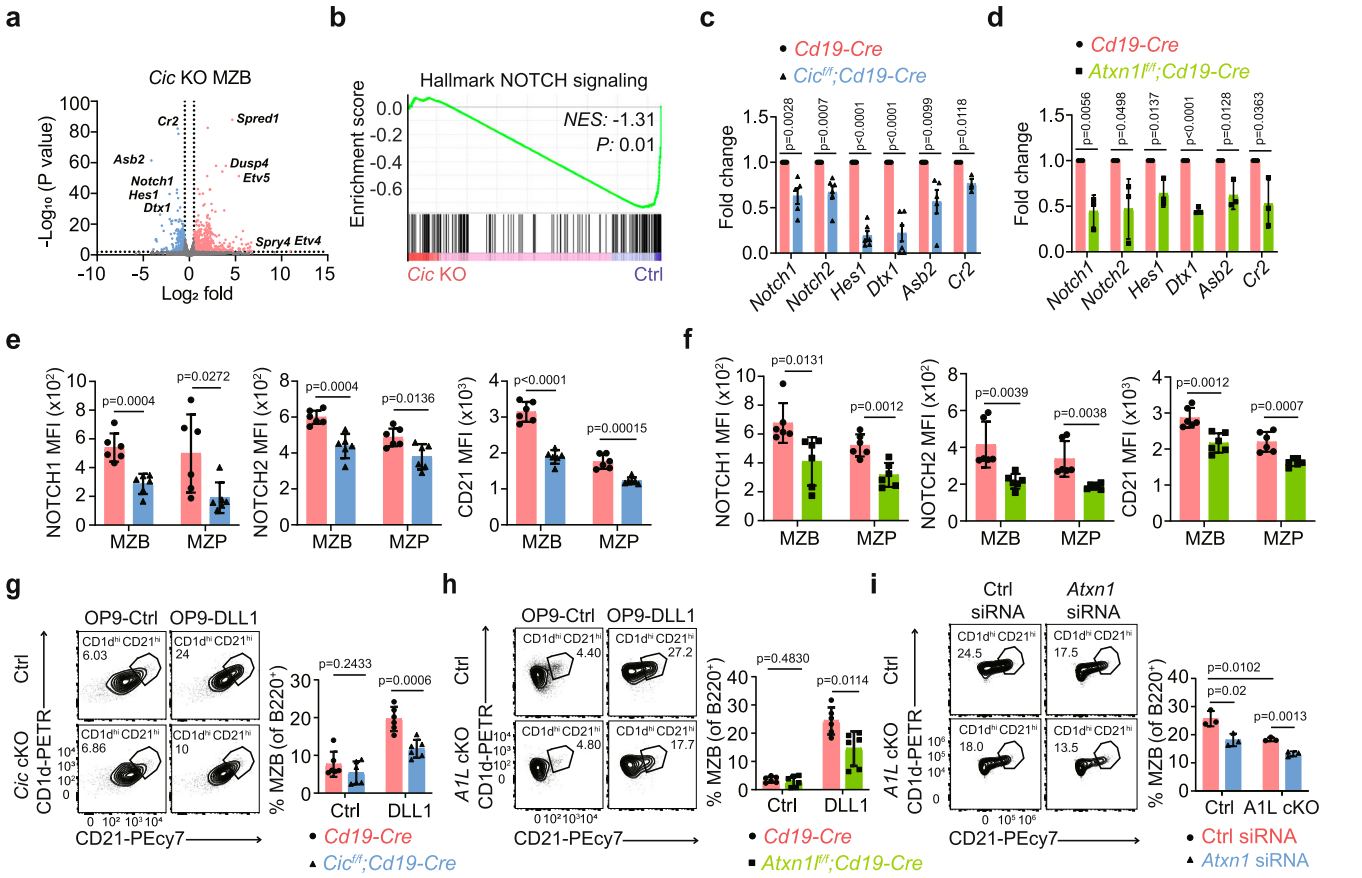

Fig. 5 | Notch signaling is downregulated by CIC-ATXN1L complex deficiency. **a** Volcano plots showing differentially expressed genes (DEGs, $\log_2$ fold-change > 0.5) in *Cic*-deficient MZB cells. Two samples of each genotype were subjected to RNA sequencing. Downregulated Notch signaling-related genes and upregulated CIC target genes are shown next to each corresponding dot. **b** Gene set enrichment analysis (GSEA) of DEGs in *Cic*-deficient MZB cells. The gene set database HALLMARK_NOTCH_SIGNALING (MM3870) was employed for GSEA. RT-qPCR analysis showing the downregulation of Notch signaling-related genes in *Cic*-null (**c**) and *Atxn1l*-null (**d**) MZB cells. For *Notch1* and *Asb2* levels, $N = 5$ per group; for *Notch2*, *Dtx1*, and *Hes1* levels, $N = 6$ per group; and for *Cr2* levels, $N = 3$ per group (**c**). N = 3 per group (**d**). **e** Surface expression levels of NOTCH1, NOTCH2, and CD21 in MZB and MZP cells from *Cd19-Cre* and *Cic*$^{f/f}$*;Cd19-Cre* mice. $N = 6$ per group. **f** Surface expression levels of NOTCH1, NOTCH2, and CD21 in MZB and MZP cells from *Cd19-Cre* and *Atxn1l*$^{f/f}$*;Cd19-Cre* mice. $N = 6$ per group. The MFIs for NOTCH1, NOTCH2, and CD21 were determined using flow cytometry. In vitro MZB cell differentiation assay to assess the differentiation potential of *Cic*-null (**g**) and *Atxn1l*-null (**h**) T1B cells into MZB cells. Sorted T1B cells were co-cultured with either control or DLL1-expressing OP9 cells for 72 h and subjected to flow cytometry to determine the frequency of MZB (CD21^{hi}CD1d^{hi}) cells. $N = 6$ per group. **i** In vitro MZB cell differentiation assay using control and *Atxn1l*-null T1B cells transfected with either control or *Atxn1* siRNAs. T1B cells were co-cultured with DLL1-expressing OP9 cells for 72 h. $N = 3$ per group. Data represent 2–3 independent experiments. Statistics: Kolmogorov–Smirnov test (**b**) and two-tailed Student's *t*-test (**c**–**i**). Bar graphs present the data as mean ± S.D. Ctrl: *Cd19-Cre*, Cic cKO: *Cic*$^{f/f}$*;Cd19-Cre*, and A1L cKO: *Atxn1l*$^{f/f}$*;Cd19-Cre*. MZB marginal zone B cells, CIC capicua, RT-qPCR quantitative real-time polymerase chain reaction, MZP marginal zone progenitor cells, MFI mean fluorescence intensity, and NES normalized enrichment score. Source data are provided as a Source Data file.

effects in *Cic*$^{f/f}$*;Cd19-Cre* mice (Fig. 7c–e). However, the serum anti-OVA IgM levels were significantly restored in *Etv4*$^{-/-}$*;Cic*$^{f/f}$*;Cd19-Cre* mice (Fig. 7e), suggesting that the impaired IgM production observed in *Cic*$^{f/f}$*;Cd19-Cre* mice following TD antigen immunization was primarily attributed to MZB cell development defects.

We also investigated the LPS-induced sepsis progression in control, *Cic*$^{f/f}$*;Cd19-Cre*, and *Etv4*$^{-/-}$*;Cic*$^{f/f}$*;Cd19-Cre* mice. All control and *Etv4*$^{-/-}$*;Cic*$^{f/f}$*;Cd19-Cre* mice succumbed to sepsis within 72 h after LPS injection, whereas over 50% of *Cic*$^{f/f}$*;Cd19-Cre* mice survived (Fig. 7f). The diminished IL-6 production and immune cell infiltration into lung tissues observed in *Cic*$^{f/f}$*;Cd19-Cre* mice were significantly restored in *Etv4*$^{-/-}$*;Cic*$^{f/f}$*;Cd19-Cre* mice (Fig. 7g, h). These results demonstrate that the mitigation of LPS-induced sepsis progression in *Cic*$^{f/f}$*;Cd19-Cre* mice is caused by defects in MZB cell development.

Discussion

This study investigated the role of CIC and its binding partners, ATXN1 and ATXN1L, in B-2 cell development (Fig. 8). T2B and FOB cell populations were substantially decreased in *Cic*$^{f/f}$*;Cd19-Cre* mice, whereas *Atxn1*$^{-/-}$ and *Atxn1l*$^{f/f}$*;Cd19-Cre* mice did not exhibit these alterations. This suggests that CIC destabilization caused by the absence of either ATXN1 or ATXN1L may be insufficient to disrupt T2B and FOB cell development. In most tissues and cell types, ATXN1L plays a dominant role in stabilizing CIC compared with ATXN1[30,31]. Consistent with this information, the reduction in MZB cell population was greater in *Atxn1l*$^{f/f}$*;Cd19-Cre* mice (Fig. 1b) than in *Atxn1*$^{-/-}$ mice (Supplementary Fig. S1d) when compared with their respective control mice. However, the expansion of B-1 cell populations, observed in both *Cic*$^{f/f}$*;Cd19-Cre* and *Atxn1*$^{-/-}$ mice, was not evident in *Atxn1l*$^{f/f}$*;Cd19-Cre* mice, suggesting that CIC stability may be primarily ensured by ATXN1 rather than ATXN1L in B-1 cells.

Our study uncovered the molecular mechanisms underlying the defect in MZB cell development caused by CIC-ATXN1L complex deficiency. *Etv4* was the CIC target gene that downregulated Notch signaling in *Cic*-null and *Atxn1l*-null MZP and MZB cells. ETV4 also functions as a transcriptional repressor for *Notch1* and *Notch2* expression in a cell-type-specific manner. Consistent with this result, previous studies have shown that ETV4 overexpression downregulates

https://doi.org/10.1038/s41467-024-54803-z

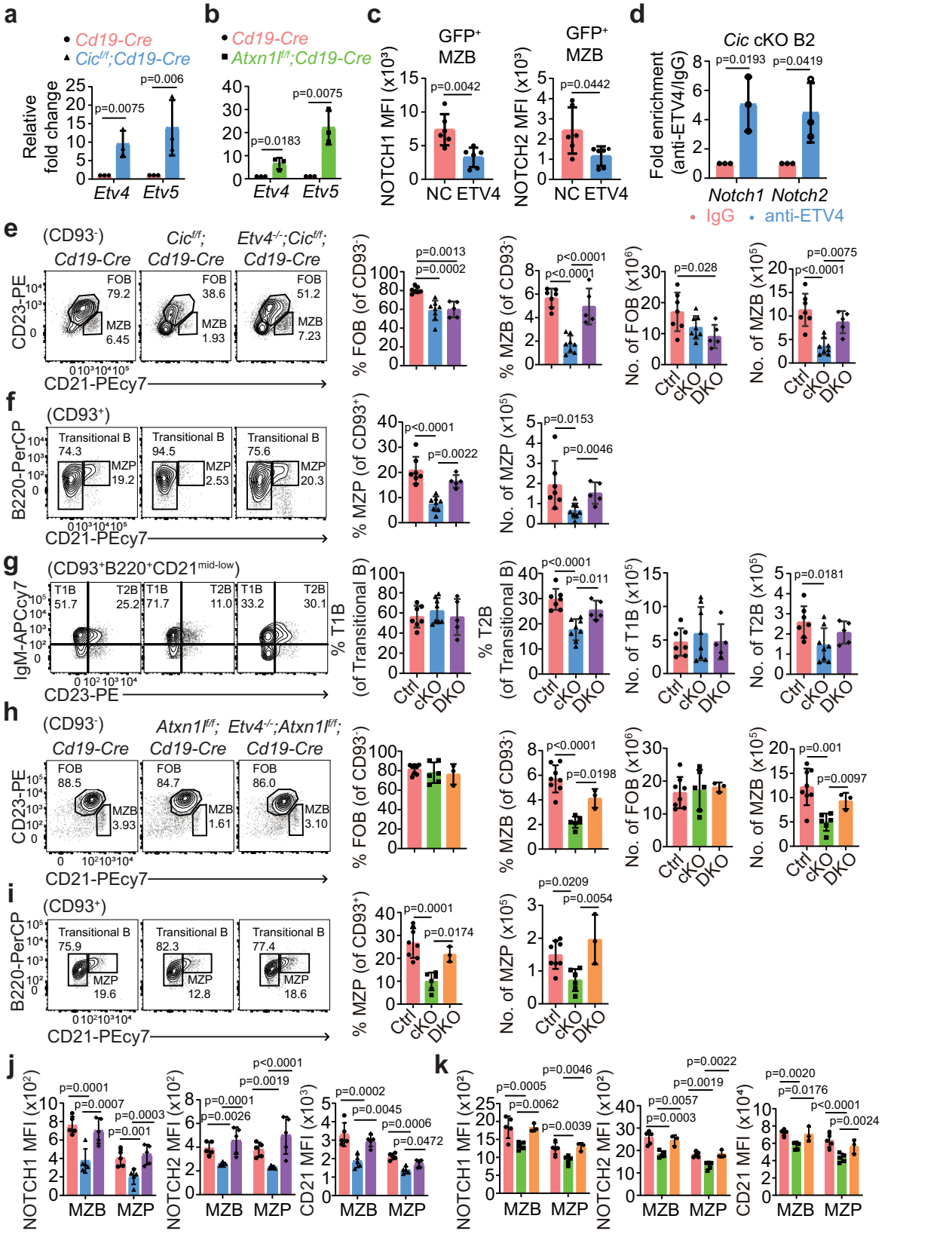

NOTCH1 expression and upregulates *NOTCH2* expression in MDA-MB-231 breast cancer cells[50]. Many transcription factors play a dual role as transcriptional activators and repressors, depending on their interacting coactivators and corepressors[51]. Therefore, identifying corepressors that interact with ETV4 and are recruited to *Notch1* and *Notch2* loci during MZB cell development would be crucial for further understanding the dysregulation of MZB cell development caused by a deficiency in the CIC-ATXN1/ATXN1L complex.

The regulation of Notch signaling by the CIC-ATXN1/ATXN1L complex may involve additional molecular mechanisms beyond ETV4 de-repression. The phosphoinositide-3-kinase (PI3K)-AKT pathway is known to induce Notch-dependent responses in various cell types,

Fig. 6 | *Etv4* is a CIC target gene that suppresses Notch signaling and MZB cell development. RT-qPCR analysis of *Etv4* and *Etv5* levels in MZB cells from *Cic$^{f/f}$;Cd19-Cre* (**a**) and *Atxn1l$^{f/f}$;Cd19-Cre* (**b**) mice. $N = 3$ per group. **c** Flow cytometry of NOTCH1 and NOTCH2 levels in MZB cells infected with either a control (NC) or ETV4-expressing (ETV4) retrovirus. $N = 6$ per group. **d** ChIP-qPCR analysis of the *Notch1* and *Notch2* promoter regions containing ETV4 binding motifs. B-2 cells isolated from the spleens of *Cic$^{f/f}$;Cd19-Cre* mice were subjected to ChIP using either IgG or an anti-ETV4 antibody. $N = 3$ per group. Flow cytometry of splenic FOB and MZB cells (**e**), MZP cells (**f**), and T1B and T2B cells (**g**) in *Cd19-Cre*, *Cic$^{f/f}$;Cd19-Cre*, and *Etv4$^{-/-}$;Cic$^{f/f}$;Cd19-Cre* mice. $N = 7$ for *Cd19-Cre*, $N = 8$ for *Cic$^{f/f}$;Cd19-Cre*, and $N = 5$ for *Etv4$^{-/-}$;Cic$^{f/f}$;Cd19-Cre*. Ctrl: *Cd19-Cre*, cKO: *Cic$^{f/f}$;Cd19-Cre*, and DKO: *Etv4$^{-/-}$;Cic$^{f/f}$;Cd19-Cre*. Flow cytometry of splenic FOB and MZB cells (**h**) and MZP cells (**i**) in *Cd19-Cre*, *Atxn1l$^{f/f}$;Cd19-Cre*, and *Etv4$^{-/-}$;Atxn1l$^{f/f}$;Cd19-Cre* mice. $N = 8$ for *Cd19-Cre*, $N = 6$ for *Atxn1l$^{f/f}$;Cd19-Cre*, and $N = 3$ for *Etv4$^{-/-}$;Atxn1l$^{f/f}$;Cd19-Cre*. Ctrl: *Cd19-Cre*, cKO: *Atxn1l$^{f/f}$;Cd19-Cre*, and DKO: *Etv4$^{-/-}$;Atxn1l$^{f/f}$;Cd19-Cre*. **j** Surface expression levels of NOTCH1, NOTCH2, and CD21 in MZB and MZP cells from *Cd19-Cre*, *Cic$^{f/f}$;Cd19-Cre*, and *Etv4$^{-/-}$;Cic$^{f/f}$;Cd19-Cre* mice. $N = 5$ per group. **k** Surface expression levels of NOTCH1, NOTCH2, and CD21 in MZB and MZP cells from *Cd19-Cre*, *Atxn1l$^{f/f}$;Cd19-Cre*, and *Etv4$^{-/-}$;Atxn1l$^{f/f}$;Cd19-Cre* mice. $N = 5$ for *Cd19-Cre* and *Atxn1l$^{f/f}$;Cd19-Cre*, and $N = 3$ for *Etv4$^{-/-}$;Atxn1l$^{f/f}$;Cd19-Cre*. The MFIs for NOTCH1, NOTCH2, and CD21 were determined using flow cytometry. Data represent 2–3 independent experiments. Statistics: two-tailed Student's *t*-test (**a**–**d**) and one-way ANOVA with Tukey's multiple comparisons test (**e**–**k**). Bar graphs present data as mean ± S.D. RT-qPCR quantitative real-time polymerase chain reaction, FOB follicular B cells, MZB marginal zone B cells, MZP marginal zone progenitor cells, and MFI mean fluorescence intensity. Source data are provided as a Source Data file.

including cancer and immune cells[52–55]. Moreover, Notch signaling can activate the PI3K-AKT pathway through an autocrine loop[56]. Given the decreased phospho-AKT levels in *Cic*-null FOB cells, the downregulation of this pathway might contribute to the CIC deficiency-mediated reduction in Notch signaling. On the other hand, it is known that ATXN1 and ATXN1L interact with RBP-J, a key Notch signaling mediator[10], and recruit SMRT and HDAC3 to repress the expression of Notch target genes in mammalian cells[57]. The interaction between RBP-J and ATXN1 or ATXN1L is disrupted by NCID overexpression, leading to the activation of Notch target genes[57]. Since CIC deficiency destabilizes ATXN1 and ATXN1L[30], it is plausible that not only ATXN1L deficiency but also CIC deficiency can enhance RBP-J-mediated activation of Notch signaling. Therefore, the downregulation of Notch signaling observed in *Cic*-null and *Atxn1l*-null MZB cells might be the result of these complex molecular alterations.

T2B cells develop into FOB and MZB cells, of which MZB cells specifically require Notch signaling[4]. *Etv4$^{-/-}$;Cic$^{f/f}$;Cd19-Cre* mice showed that the frequency of T2B cells was restored but the FOB cell population was not (Fig. 6d–f), suggesting that the decrease in FOB cell population was not primarily due to defective T2B cell development in *Cic$^{f/f}$;Cd19-Cre* mice. We found that BCR signaling was significantly attenuated in *Cic*-null FOB cells. However, our previous study has shown that it was enhanced in *Cic*-null T2B cells[43]. Similarly, developmental stage-specific attenuation of T cell receptor signaling caused by CIC deficiency has been reported[38]. The de-repression of CIC target genes that negatively regulated the RAS-MAPK pathway, including *Spry4*, *Spred1*, *Dusp4*, and *Dusp6*, was proposed as the molecular mechanism behind this phenomenon[38]. Therefore, we speculate that the impaired FOB cell formation in *Cic$^{f/f}$;Cd19-Cre* mice may result from the attenuation of BCR signaling potentially caused by the de-repression of CIC target genes such as *Spry4*, *Spred1*, *Spred2*, and *Dusp4*, which were observed to be significantly upregulated in *Cic*-null FOB cells[43]. T2B cells are normally formed in mice deficient in RBP-J, suggesting that the decreased T2B cell population in *Cic$^{f/f}$;Cd19-Cre* mice is not caused by a downregulation of Notch signaling. The observed restoration of T2B cell frequency in *Etv4$^{-/-}$;Cic$^{f/f}$;Cd19-Cre* mice (Fig. 6f) warrants further investigation to elucidate the molecular mechanism underlying the suppression of T2B cell formation via ETV4 overexpression.

MZB cell function conventionally involves protection against blood-borne pathogens via the expression of polyreactive BCRs that bind to multiple microbial molecular patterns. Hence, MZB cells are regarded as innate-like B cells, which mediate the frontline defense against blood-borne microorganisms[16]. Conversely, MZB cells can exacerbate the progression of LPS- or bacteria-induced sepsis in mice by secreting IL-6[22,25]. While the conventional innate-like features of MZB cells are well-understood, their role in sepsis has not received much attention. Our study confirmed their sepsis-promoting function by assessing sepsis severity in *Cic$^{f/f}$;Cd19-Cre* and *Atxn1l$^{f/f}$;Cd19-Cre* mice following LPS treatment. Furthermore, the MZB cell population was restored via the deletion of *Etv4* alleles, which reversed the attenuation of sepsis progression observed in *Cic$^{f/f}$;Cd19-Cre* mice, highlighting the pivotal role of MZB cells in sepsis. However, it remains elusive whether MZB cells promote sepsis progression in humans. Although our study suggests that the CIC-ATXN1/ATXN1L complex and ETV4 are potential therapeutic targets for sepsis, further research is required to investigate the role of human MZB cells in sepsis and the involvement of the CIC-ATXN1/ATXN1L complex in MZB cell development in humans.

Methods

Mice

Cic floxed[40,58] (#030555, Jackson Laboratory, USA), *Vav1-Cre*[59] (#035670, Jackson Laboratory), *Cd19-Cre*[60] (#006785, Jackson Laboratory), *Atxn1*$^{-/-}$[61] (#029025, Jackson Laboratory), and *Atxn1l* floxed[62] (#030717, Jackson Laboratory) mice were generated as described previously. Whole-body *Etv4*$^{-/-}$ mice were generated using the CRISPR/Cas9 system (Korea Mouse Phenotyping Center, Seoul, Korea). All mice were maintained on a C57BL/6 background. All experiments were conducted with 8–10-week-old mice unless otherwise indicated. For the experimental sepsis model, 8–12-week-old female mice were used. Animals were maintained in a specific pathogen-free animal facility under a standard 12:12 h light/dark cycle and administered standard rodent chow and water *ad libitum*. All animal procedures performed in this study were ethically approved by the Institutional Animal Care and Use Committee of Pohang University of Science and Technology.

Flow cytometry

Immune cells were obtained from the peritoneal cavity and spleen. The spleen tissue was ground using a Tenbroeck Tissue Grinder (Cat: 357424, WHEATON®, DWK Life Sciences, Wertheim, Germany) to obtain single cells. Red blood cells were removed using RBC lysis buffer (155 mM NH_4Cl, 12 mM $KHCO_3$, and 0.1 mM EDTA). Peritoneal cavity cells were harvested using a syringe by injecting 5 ml phosphate-buffered saline (PBS) into the cavity and shaking for 1 min. The process was repeated twice. Ghost Dye™ Violet 510 viability dye (1:1000 dilution, Cat: 13-0870, Tonbo Biosciences, CA, USA) was used to differentiate viable from dead cells. For surface staining, the following antibodies were used at a 1:300 dilution: anti-B220-PerCP (Cat: 103234, BioLegend, CA, USA), anti-CD19-Bv421 (Cat: 562701, BD Biosciences, NJ, USA), anti-CD21/35-PEcy7 (Cat: 25-0211-82, eBioscience, CA, USA), anti-CD23-PE (Cat: 101-607, BioLegend), anti-CD23-FITC (Cat: 101605, BioLegend), anti-CD93-FITC (Cat: 136507, BioLegend), anti-CD93-APC (Cat: 17-5892-81, BioLegend), anti-IgM-APC-eFluor® 780 (Cat: 47-5790-80, eBioscience), anti-NOTCH2-APC (Cat: 130713, BioLegend), anti-NOTCH1-PE (Cat: 130607, BioLegend), anti-CD138-BV421 (Cat: 142507, BioLegend), anti-CD5-PE (Cat: 553023 BD Biosciences), anti-CD43-FITC (Cat: 143204, BioLegend), anti-CD1d-PEdazzle594 (Cat: 123519 BioLegend), anti-GL7-FITC (Cat: 144611, BioLegend), anti-BAFFR-PE (Cat: 134103, BioLegend), and anti-CD24-AlexaFluor 700 (Cat: 101836, BioLegend). Monoclonal antibody anti-CD95 (FAS)-biotin (Cat: 554256, BD Biosciences) was used with Streptavidin-APC (Cat: 554067, BD

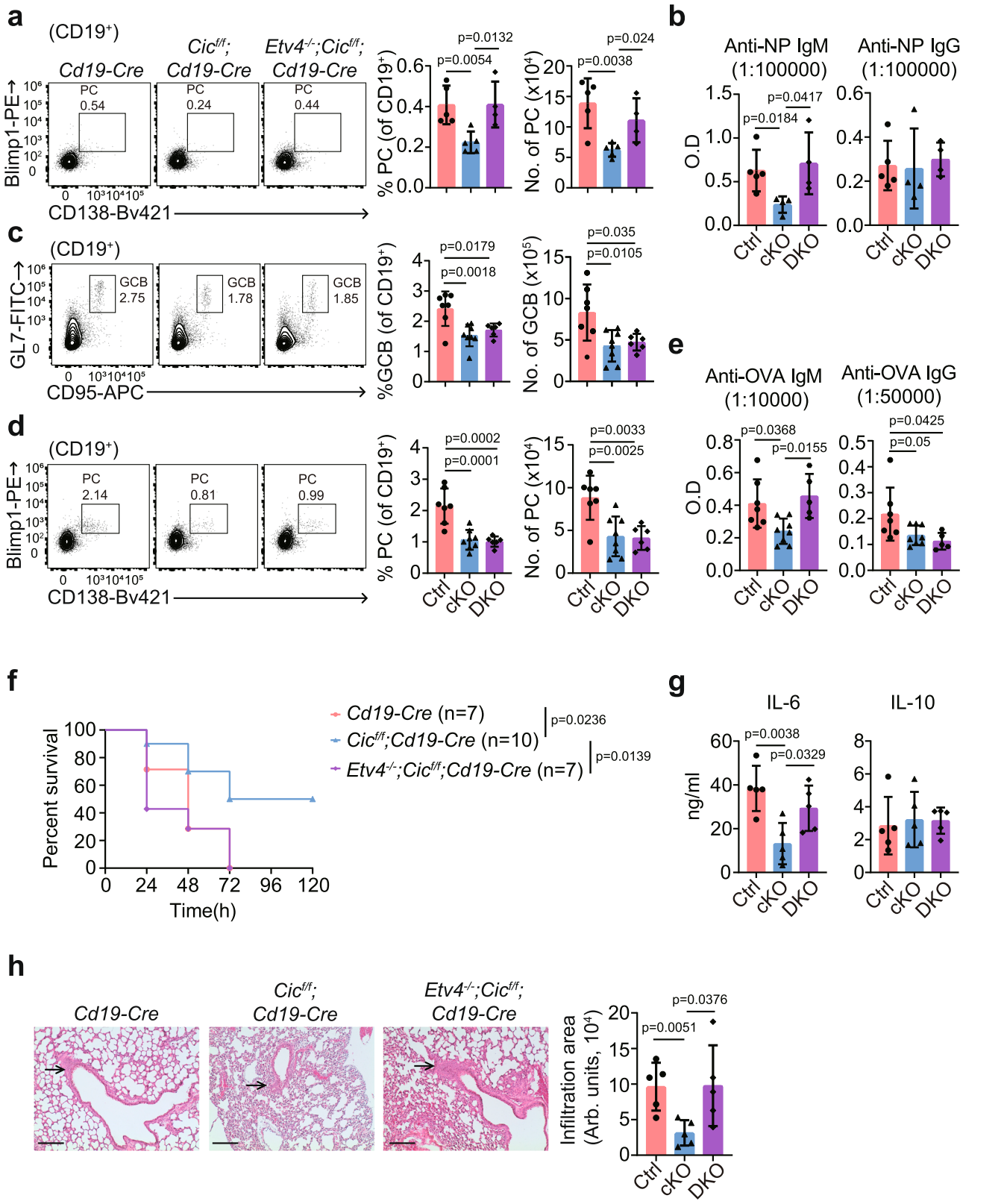

Biosciences). Surface staining was performed on ice by incubating cells with monoclonal antibody cocktails for 30 min. For intracellular staining, cells were fixed and permeabilized using the FOXP3/Transcription staining kit (Cat: 00-5523-00, eBioscience) as per the manufacturer's instructions. Permeabilized cells were stained with anti-Blimp1-PE (1:100 dilution; Cat: 150005, BioLegend) and anti-Ki-67-APC (1:100 dilution; Cat: 17-5698-82, eBioscience). All stained cells were analyzed using an LSRFortessa (BD Biosciences) or a Cytoflex (Beckman Coulter, CA, USA) flow cytometer[63]. The flow cytometry gating strategies used in this study are presented in Supplementary Fig. S8.

In vitro FOB cell differentiation assay

T2B cells ($CD19^+CD93^+B220^+CD21^{mid}CD23^+IgM^+$) from *Cd19-Cre* and *Cic$^{f/f}$;Cd19-Cre* mice were sorted using a MoFlo Astrios cell sorter

Fig. 7 | Restoration of IgM production and sepsis progression in *Etv4*$^{-/-}$;*Cic*$^{f/f}$;*Cd19-Cre* mice. a, **b** *Cd19-Cre*, *Cic*$^{f/f}$;*Cd19-Cre*, and *Etv4*$^{-/-}$;*Cic*$^{f/f}$;*Cd19-Cre* mice were immunized with NP-Ficoll for 7 days. **a** Flow cytometry of splenic plasma cells. $N = 5$ for *Cd19-Cre* and *Cic*$^{f/f}$;*Cd19-Cre*, and N = 4 for *Etv4*$^{-/-}$;*Cic*$^{f/f}$;*Cd19-Cre*. **b** Serum NP-specific IgM and IgG levels determined using ELISA. $N = 5$ for *Cd19-Cre* and $N = 4$ for *Cic*$^{f/f}$;*Cd19-Cre* and *Etv4*$^{-/-}$;*Cic*$^{f/f}$;*Cd19-Cre*. **c**–**e** *Cd19-Cre*, *Cic*$^{f/f}$;*Cd19-Cre*, and *Etv4*$^{-/-}$;*Cd19-Cre* mice were immunized with OVA in alum for 7 days. Flow cytometry of splenic GCB cells (**c**) and plasma cells (**d**). $N = 7$ for *Cd19-Cre*, $N = 8$ for *Cic*$^{f/f}$;*Cd19-Cre*, and $N = 6$ for *Etv4*$^{-/-}$;*Cic*$^{f/f}$;*Cd19-Cre*. **e** Serum OVA-specific IgM and IgG levels determined using ELISA. $N = 7$ for *Cd19-Cre*, $N = 8$ for *Cic*$^{f/f}$;*Cd19-Cre*, and $N = 5$ for *Etv4*$^{-/-}$;*Cic*$^{f/f}$;*Cd19-Cre*. **f**–**h** Female *Cd19-Cre*, *Cic*$^{f/f}$;*Cd19-Cre*, and *Etv4*$^{-/-}$;*Cic*$^{f/f}$;*Cd19-Cre* mice were injected intravenously with LPS. **f** Survival rate of LPS-treated mice. Mortality was monitored every 24 h. $N = 7$ for *Cd19-Cre* and *Etv4*$^{-/-}$;*Cic*$^{f/f}$;*Cd19-Cre*, and $N = 10$ for *Cic*$^{f/f}$;*Cd19-Cre*. **g** Serum IL-6 and IL-10 levels determined using ELISA. **h** Histology of immune cell infiltration into lung tissue. Arrows indicate immune cell-infiltrated regions. Scale bar: 100 μm. Serum samples and lung tissues were collected from the mice 12 h after LPS injection. $N = 5$ per group. Data represent 2–3 independent experiments. Statistics: one-way ANOVA with Tukey's multiple comparisons test (**a**–**e**, **g**–**h**) and Log-rank (Mantel-Cox) test (**f**). The bar graph presents data as mean ± S.D. Ctrl: *Cd19-Cre*, cKO: *Cic*$^{f/f}$;*Cd19-Cre*, and DKO: *Etv4*$^{-/-}$;*Cic*$^{f/f}$;*Cd19-Cre*. ELISA enzyme-linked immunosorbent assay, OVA ovalbumin, and GCB germinal center B cell. Source data are provided as a Source Data file.

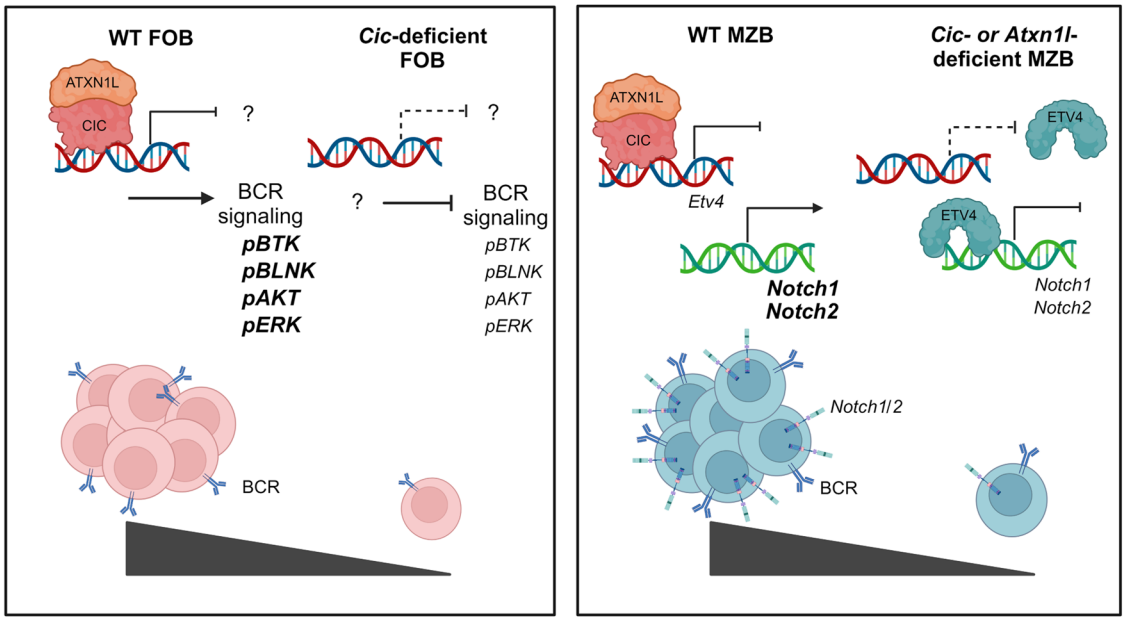

Fig. 8 | The CIC-ATXN1L complex regulates B-2 cell development. A schematic diagram illustrates the role of the CIC-ATXN1L complex in B-2 cell development. The left panel shows that CIC deficiency reduces the formation of FOB cells by downregulating BCR signaling. The specific CIC target genes involved in this process have not yet been identified. The right panel indicates that the deficiency of either CIC or ATXN1L downregulates NOTCH1 and NOTCH2 expression by de-repressing ETV4, leading to a decreased MZB cell population. The diagram was created using BioRender.com, which permits the reuse of its content under a CC-BY 4.0 Attribution 4.0 International license.

(Beckman Coulter). The sorted cells were cultured in Rosewell Park Memorial Institute 1640 (RPMI 1640; Cat: LM011-60, Welgene Inc., Gyeongsangbuk-do, Korea) media supplemented with 10% fetal bovine serum (FBS; Cat: S001-01, Welgene Inc.) and 10 μg/ml anti-IgM F(ab)'2 (Cat: 16-5092-85, eBioscience) for 72 h. The cells were harvested and stained with a monoclonal antibody cocktail (anti-CD24 and anti-CD21). FOB cells were analyzed as CD24^{+}CD21^{+} cells.

In vitro MZB cell differentiation assay

T1B cells (CD19^{+}CD93^{+}B220^{+}CD21^{lo}CD23^{-}IgM^{+}) from *Cd19-Cre*, *Cic*$^{f/f}$;*Cd19-Cre*, and *Atxn1l*$^{f/f}$;*Cd19-Cre* mice were sorted using a MoFlo Astrios cell sorter. The sorted cells were co-cultured with either control or DLL1-expressing OP9 cells in RPMI 1640 media supplemented with 10% FBS and 20 ng/ml of BAFF cytokine (Cat: 8876-BF-010, R&D Systems, MA, USA). After 72 h, the cells were harvested and stained with a monoclonal antibody cocktail (anti-CD1d and anti-CD21). MZB cells were analyzed as CD1d^{hi}CD21^{+} cells.

BCR signaling analysis

To measure IgM stimulated BCR signaling, splenocytes were stimulated with 10 μg/ml anti-IgM F(ab)'2 for 5 min in a 37 °C heat block and then washed with cold PBS to stop the activation of BCR signaling. The activated cells were then fixed with Cytofix/Cytoperm™ (Cat: 554655, BD Biosciences) for 30 min and washed with cold PBS. Cells were suspended in ice-cold methanol for cytoplasm permeabilization. After washing with PBS, cells were stained with either anti-p-BTK-PE (Cat: 646903, BioLegend), anti-pBLNK PE (Cat: 558442, BD Biosciences), anti-pERK-PE (Cat: 12-9109-41, Invitrogen, CA, USA), or anti-pAKT-PE (Cat: 560378, BD Biosciences) on ice for 1 h. To measure tonic BCR signaling, cells were immediately permeabilized with ice-cold methanol without anti-IgM treatment. All stained cells were analyzed using an LSRFortessa or a Cytoflex flow cytometer.

In vitro apoptosis assay

The apoptosis assay was performed as previously described[43,64]. FOB (CD19^{+}CD93^{-}CD21^{int}CD23^{+}) and MZB (CD19^{+}CD93^{-}CD21^{hi}CD23^{lo}) cells from *Cd19-Cre*, *Atxn1l*$^{f/f}$;*Cd19-Cre*, and *Cic*$^{f/f}$;*Cd19-Cre* mice were sorted using a MoFlo Astrios cell sorter. Sorted cells were cultured in RPMI 1640 media supplemented with 10% FBS, 1% β-mercaptoethanol (Cat: 21985-023, Gibco, Thermo Fisher Scientific, MA, USA), and 1% penicillin-streptomycin (Cat: 15140122, Gibco). After 72 h, the cells were harvested and stained with an Annexin V-PI staining kit (Cat: 640932, BioLegend) as per the manufacturer's instructions. Stained cells were analyzed using an LSRFortessa or a Cytoflex flow cytometer.

Luciferase assay

Mouse *Notch1* and *Notch2* promoter regions (−1000 to −1) were amplified via PCR using Pfu-X DNA polymerase (Cat: SPX16-R250, SolGent, Daejeon, South Korea) and cloned into the pGL3-Basic firefly luciferase vector (Cat: E1751, Promega, WI, USA) using KpnI and XhoI restriction enzymes. HEK293T and HeLa cells were seeded into 24-well culture plates and co-transfected with 500 ng of the cloned firefly luciferase vector (pGL3-*Notch1* pro or pGL3-*Notch2* pro), 50 ng of a *Renilla* luciferase vector, and 400 ng of the expression vector (MIGR1, MIGR1-ETV4, or MIGR1-ETV5) using FUGENE®HD transfection reagent (Cat: E2311, Promega) as per the manufacturer's instructions. The cells were lysed 48 h after transfection, and luciferase activity was measured using the Dual-Luciferase Reporter Assay System (Cat: E1960, Promega) as per the manufacturer's instructions.

Site-directed mutagenesis

Site-directed mutagenesis was performed using a Quick-Change II XL Site-Directed Mutagenesis kit (Cat: 200521, Agilent Technologies, CA, USA) as per the manufacturer's instructions. Primers used for the mutagenesis of three ETS binding motifs in the *Notch1* promoter were as follows: Mut-1 sense, 5′-TTAACTGCAAAGGGATAAGTTAGGCATCTTGGACGCCCAG-3′ and Mut-1 antisense, 5′-CTGGGCGTCCAAGATGCCTAACTTATCCCTTTGCAGTTAA-3′; Mut-2 sense, 5′-TTTAAGGTCAAGCGTTCCGTTAGTCATGGCTAAGAGTGCC-3′ and Mut-2 antisense, 5′-GGCACTCTTAGCCATGACTAACGGAACGCTTGACCTTAAA-3′; Mut-3 sense, 5′-GTAAGGGTTCGCAGTTACCAGGGGCGGAGC-3′ and Mut-3 antisense, 5′-GCTCCGCCCCTGGTAACTGCGAACCCTTAC-3′. Primers used for the mutagenesis of two ETS binding motifs in the *Notch2* promoter were as follows: Mut-1 sense, 5′-CGCGCCCAGGGGTTAACCGCAGAAAGAAGC-3′ and Mut-1 antisense, 5′-GCTTCTTTCTGCGGTTAACCCCTGGGCGCG-3′; Mut-2 sense, 5′-GCCCGCGTGTCCTAACGCCTCGGCCTCC-3′ and Mut-2 antisense, 5′-GGAGGCCGAGGCGTTAGGACACGCGGGC-3′. Desired mutations were validated using Sanger sequencing.

RNA sequencing and data analysis

MZB cells were sorted from *Cd19-Cre* and *Cic$^{f/f}$;Cd19-Cre* mice using a MoFlo Astrios cell sorter. Total RNA was purified using RiboEx reagent (Cat: 301-002, GeneAll, Seoul, Korea) as per the manufacturer's instructions. RNA purity was determined by assaying 1 µl total RNA on a NanoDrop8000 spectrophotometer (Thermo Fisher Scientific). Total RNA integrity was evaluated using an Agilent Technologies 2100 Bioanalyzer. An mRNA sequencing library was constructed using the Truseq Stranded mRNA/Total Library Prep Kit (Illumina Inc., CA, USA) as per the manufacturer's instructions. Tophat (v2.0.13) software was used to map reads for each sample to the mm10 RefSeq reference genome. Aligned results were then added to Cuffdiff (v2.2.0) to identify DEGs. DEGs with $\log_2$ fold-change >0.5 and $P < 0.01$ were selected for GO and KEGG pathway analyses using the DAVID website (https://david.ncifcrf.gov/). The GO analysis was performed in terms of biological processes, cell components, and molecular function. GSEA was performed using GSEA software (version 4.1.0, https://gsea-msigdb.org/gsea/index.jsp). HALLMARK_NOTCH_SIGNALING (MM3870) was used as the gene set database for GSEA.

RT-qPCR

MZB cells were sorted from *Cd19-Cre*, *Cic $^{f/f}$;Cd19-Cre*, and *Atxn1l $^{f/f}$;Cd19-Cre* mice using a MoFlo Astrios cell sorter. Total RNA was purified using the RiboEx reagent and reverse-transcribed into cDNA using a GoScript Reverse Transcription System (Cat: A5004, Promega) as per the manufacturer's instructions. The SYBR Green real-time PCR master mix (Cat: TOQPK-201, Toyobo, Osaka, Japan) was used for qPCR. Gene expression levels were normalized to 18S rRNA levels. Primer sequences are shown in Supplementary Table 1.

Immunization with TI and TD antigens

Cd19-Cre, *Cic$^{f/f}$;Cd19-Cre*, and *Atxn1l$^{f/f}$;Cd19-Cre* mice aged 10–12 weeks were injected intravenously with 50 µg TNP-AECM-FICOLL (Cat: F-1300-10, LGC Biosearch Technologies, Hoddesdon, UK) or intraperitoneally with 50 µg OVA (Cat: A2512, Sigma–Aldrich, MO, USA) immersed in alum (Cat: vac-alu-250, InvivoGen, CA, USA). After 7 days, the mice were sacrificed to obtain the serum and spleen tissues. Serum samples were used to measure NP-specific or OVA-specific IgM and IgG levels. Spleen tissues were used to analyze the splenic plasma ($CD19^+CD138^+Blimp1^+$) and GCB ($CD19^+GL\text{-}7^+CD95^+$) cells.

LPS-induced sepsis

Female *Cd19-Cre*, *Cic$^{f/f}$;Cd19-Cre*, *Atxn1l$^{f/f}$;Cd19-Cre*, and *Etv4$^{-/-}$;Cic$^{f/f}$;Cd19-Cre* mice were injected intravenously with 500 µg LPS from *Escherichia coli* O55:B5 (Cat: L2880-25MG, Sigma–Aldrich). LPS-treated mice were monitored every 24 h for mortality. Those that experienced severe convulsions, loss of motor skills, or a 20% decrease in body weight were euthanized. To obtain serum samples and lung tissues, the mice were sacrificed 12 h after LPS treatment. Mouse serum samples were used to measure IL-6 and IL-10 levels. Lung tissues were utilized to prepare paraffin blocks to identify immune cell infiltration in the organ.

Hematoxylin and eosin staining

Staining was performed as previously described[40,65]. Lung samples were fixed in a 10% formalin solution (Cat: HT501320-9.5L, Sigma–Aldrich) and agitated overnight. The samples were subjected to sequential dehydration in 70%, 80%, 90%, and 100% ethanol over the following 4 days. The lung samples were then immersed in xylene for 1 h; this process was performed three times. The xylene-soaked tissue was then placed in a paraffin-containing glass vessel and placed in a 60 °C oven overnight to allow paraffin infiltration into the tissue. The next day, paraffin blocks were constructed using an embedding machine (Shandon Histocentre 3, Thermo Fischer Scientific). Tissue sections were prepared using a Semi-Automated Rotary Microtome (Cat: RM2245, Leica Biosystems, Wetzlar, Germany). Sectioned tissues were mounted on non-adherent slides and air-dried on a 50 °C heat plate overnight. Paraffin on the slides was removed via triple immersion in xylene at 7-min intervals. Dehydrated lung tissue sections were rehydrated via sequential immersion in bottles containing 100%, 90%, 80%, and 70% ethanol at 3-min intervals. The sections were then incubated in hematoxylin (Cat: GT0111, Glentham, Life Sciences Ltd., Wiltshire, UK) for 1 min for nuclear staining. The slides were then rinsed with tertiary distilled water and incubated in a 0.1% ammonium hydroxide solution (Cat: 221228, Sigma–Aldrich) for 1 min to complete nuclear staining. After the bluing reaction, the slides were washed with tertiary distilled water and incubated in eosin (Cat: EM000G-5, Cancer Diagnostics, NC, USA) for 1 min to stain the cytoplasm. After cell staining, Canadian balsam solution (Cat: C1795, Sigma–Aldrich) was applied directly onto the lung tissue, and a cover glass was placed over it. The 100× images of the lung sections were obtained using an Olympus BX41TF light microscope (Olympus Corporation, Tokyo, Japan). The immune cell-infiltrated area was quantified using ImageJ software (National Institutes of Health).

Enzyme-linked immunosorbent assay

IL-6 and IL-10 levels in serum samples were quantified using the IL-6 and IL-10 Mouse Uncoated enzyme-linked immunosorbent assay (ELISA) Kits (Cat: 88-7064-22 and 88-7105-22, Invitrogen), respectively. Antibodies captured from the kits were coated onto 96-well half-area clear flat-bottom plates (Cat: 3690, Corning Inc., NY, USA) overnight at 4 °C. The plates were then rinsed with ELISA wash buffer (0.05% Tween-20 in PBS), followed by a 1-h blocking step at room temperature. The reference cytokines and diluted serum samples were

incubated in the plates for 2 h at room temperature. The plates were then subjected to several washes and incubated with detection antibodies for 1 h at room temperature. Following additional washing, streptavidin-HRP was added and incubated for 30 min at room temperature. After washing the plates, 50 µl TMB substrate was added, and the plates were incubated for 15 min in a light-blocked environment. Finally, 50 µl of 1 M H_2SO_4 was added to stop the reaction. Optical density was measured at 450 nm using a spectrophotometer. For the NP-specific Ig ELISA, NP-BSA (Cat: T-5050-10, Biosearch Technologies) was used as the coating antigen. For OVA-specific Ig ELISA, OVA was the coating antigen used. Goat Anti-Mouse IgM, Human ads-HRP (Cat: 1020-05-SBA, Southern Biotech, AL, USA) and Goat Anti-Mouse IgG, Human ads-HRP (Cat: 1031-05-SBA, Southern Biotech) were used as secondary antibodies to capture anti-IgM and anti-IgG in serum, respectively. The overall process was consistent with that of cytokine ELISAs.

Retrovirus preparation

Plat E cells were seeded in 100 mm dishes at a density of ~2×10^6 cells. After 24 h, when the cells reached 70–80% confluency, they were co-transfected with either 4.5 µg of MIGR1 (negative control) or MIGR1-ETV4 expression vector, along with 1.5 µg of the pCL-Eco vector (retrovirus packaging vector), using FUGENE transfection reagent (Cat: E2312, Promega) according to the manufacturer's instructions. The transfected cells were incubated for 48 h at 37 °C in a humidified atmosphere containing 5% CO_2. Afterward, the cell culture supernatant containing the retrovirus particles was collected. The supernatant was mixed with Retro-X concentrator (Cat: 631456, Takara) at a 3:1 ratio and incubated overnight at 4 °C with gentle swirling. The viral mixture was then centrifuged at 1500 × *g* for 45 min at 4 °C, and the resulting virus pellet was resuspended in RPMI medium.

Retroviral transduction

B-2 cells were isolated from the spleens of WT mice using negative selection. The isolated B-2 cells were then stimulated with anti-IgM (1 µg/ml) and anti-CD40 (1 µg/ml; Cat: 553788, BD bioscience) antibodies for 18 h. For retroviral transduction, the stimulated B-2 cells were mixed with polybrene at a final concentration of 8 µg/ml and the previously prepared retrovirus stock. The cell-virus mixture was then transferred to a 24-well plate, and spin infection was performed by centrifuging the plate at 750 × *g* for 2 h at room temperature. After spin infection, the medium containing the virus mixture was carefully replaced with fresh RPMI medium to maintain cell viability. The infected cells were then cultured for 48 h at 37 °C in a 5% CO_2 incubator. Following the 48-h culture period, the cells were harvested and prepared for flow cytometry.

ChIP-qPCR

B-2 cells were isolated from the spleens of *Cic*$^{f/f}$*;Cd19-Cre* mice using negative selection. 5×10^6 B-2 cells were cross-linked with 1% paraformaldehyde for 20 min under constant agitation. To terminate the cross-linking reaction, 1 M glycine was added, followed by a 5 min incubation. The cross-linked chromatin was rinsed at least twice with cold PBS, then centrifuged at 4200 rpm for 5 min. The pellet was resuspended in Buffer 1 (50 mM HEPES-KOH, pH 7.5; 140 mM NaCl; 1 mM EDTA, pH 8.0; 10% glycerol; and 0.5% NP-40) and rotated at 4 °C for 10 min to lyse the nuclei. After a 5 min centrifugation at 4200 rpm, the pellet was resuspended in MNase digestion buffer (100 mM Tris-HCl, pH 8.0; 2 mM $CaCl_2$; 0.4% Triton X-100; and MNase [0.001 U/mL, Sigma]) and incubated at 37 °C for 12 min. The reaction was terminated by adding 10 mL of 0.5 M EDTA, followed by centrifugation at 4200 rpm for 5 min. The lysate was then resuspended in Buffer 2 (10 mM Tris-HCl, pH 8.0; 300 mM NaCl; 0.1% sodium deoxycholate; 1% Triton X-100; 1 mM EDTA, pH 8.0; and 0.5 mM EGTA, pH 8.0) and sonicated to shear DNA fragments. Sonication process is comprised with 15 cycles of 30 s eruption and 30 s resting. The supernatant was collected after micro centrifugation at 9400 rpm for 10 min at 4 °C and 10% were stored at −80 °C for input sample. For immunoprecipitation, chromatin was precleared with protein G agarose (Cat: 16-266, Merck, Darmstadt, Germany) in Buffer 2 for 90 min. Post-preclearing, 2 µg of either normal rabbit IgG (Cat: #2729, Cell Signaling Technology, MA, USA) or anti-ETV4 antibody (Cat. 10684-1-AP, Proteintech, IL, USA) was added to the samples, followed by overnight incubation at 4 °C with gentle agitation. The chromatin-antibody complexes were incubated with protein G agarose for an additional 3.5 h at 4 °C. Subsequently, the samples were washed sequentially with low salt buffer (4 mM EDTA, 2% Triton X-100, 40 mM Tris-HCl, pH 8.0, 300 mM NaCl, 0.2% SDS), high salt buffer (4 mM EDTA, 2% Triton X-100, 40 mM Tris-HCl, pH 8.0, 1 M NaCl, 0.2% SDS), LiCl buffer (0.5 M LiCl, 20 mM Tris-HCl, pH 8.0, 2 mM EDTA, 2% NP-40, 2% sodium deoxycholate), and TE buffer (20 mM Tris-HCl, pH 8.0, 2 mM EDTA). Bound chromatin was eluted with elution buffer (0.1 M $NaHCO_3$ and 0.5% SDS) and reverse-crosslinked with 200 mM NaCl at 65 °C overnight. RNA and proteins were subsequently digested with RNase A and protease K, respectively, and DNA was purified using the Expin CleanUp SV kit (Cat. 113-150, GeneAll). The qPCR primer sequences for the promoter regions of *Notch1* and *Notch2* were as follows: For *Notch1*, the forward primer sequence was 5′-CGAACTCCCTTCTACAGAGGC-3′ and the reverse primer sequence was 5′-CTGGGAGCTGTTTGGTCTCG-3′. For *Notch2*, the forward primer sequence was 5′-GTACGGGGTGCTGCTCACTC-3′ and the reverse primer sequence was 5′-AGGGGTTTCCCGCAGAAAGA-3′.

Western blotting

Using WT C57BL/6 mice, FOB and MZB cells were obtained from the spleen, and B-1a cells were obtained from the peritoneal cavity. Sorted cells were lysed in RIPA buffer (50 mM Tris-HCl [pH 7.4], 150 mM NaCl, 1 mM PMSF, 1% NP-40, 0.5% sodium deoxycholate, 0.1% SDS, 2X Complete Protease Inhibitor Cocktail [Cat: 5892953001, Roche, Basel, Switzerland], and 10X PhosSTOP™ [Cat: 4906837001, Roche]). Protein samples were separated using SDS-PAGE with 8% acrylamide gel as the separating gel. For CIC detection, SDS solution was added during the membrane transfer step. The following primary antibodies were used for protein detection: anti-CIC (1:2,000)[66], anti-ATXN1L (1:2,000)[66], anti-ATXN1 (1:2000; Cat: 2177, Cell Signaling Technology), and anti-GAPDH (1:2,000; Cat: sc-32233, Santa Cruz Biotechnology, TX, USA). Proteins were visualized using Clarity Western ECL Substrate (Cat: BR170-5061, Bio-Rad, CA, USA). Western blots were imaged using the ImageQuant LAS 500 system (GE Healthcare Life Sciences, IL, USA).

siRNA electroporation

siRNA electroporation of T1B cells was performed using the 4D-Nucleofector® X Unit (Cat: AAF-1003X, Lonza, Basel, Switzerland) with the P4 Primary Cell 4D-Nucleofector X Kit S (Cat: V4XP-4032, Lonza). T1B cells, isolated from *Cd19-Cre* and *Atxn1l*$^{f/f}$*;Cd19-Cre* mice, were resuspended in 20 µl of nucleofection mixture (comprising 14.9 µl nucleofector solution, 3.6 µl supplement solution, and 1.5 µl siRNA at 20 pmol/µl). The cell mixture (20 µl) was then transferred to a cuvette provided in the kit, and electroporation was conducted using the DI-100 program (optimized for mouse B cells). Subsequently, the T1B cells were transferred to a plate pre-seeded with OP9-DLL1 for in vitro MZB cell differentiation. After 72 h, the cells were harvested and analyzed using flow cytometry. The following siRNA sequences were used: siATXN1-sense: 5′-CUGUAUCCAGAUUACUGUATT-3′, siATXN1-antisense: 5′-UACAGUAAUCUGGAUACAGTT-3′, siNC-sense: 5′-CCUACGCCACCAAUUUCGUTT-3′, siNC-antisense: 5′-ACGAAAUUGGUGGCGUAGGTT-3′.

Statistical analysis

All experiments were performed at least two times independently. Datasets were analyzed using the two-tailed Student's *t*-test, one-way

ANOVA with Tukey's multiple comparisons test, and Log-rank (Mantel-Cox) test using Prism 10.0 software (GraphPad). Kolmogorov–Smirnov test was used for the GSEA. A $P < 0.05$ was considered significant. In the bar graphs, bars and error bars indicate mean and S.D., respectively. In the box and whisker plots, the box indicates the median and 25th–75th percentiles, while whiskers represent the 2.5th–97.5th percentiles.

Reporting summary

Further information on research design is available in the Nature Portfolio Reporting Summary linked to this article.

Data availability

The sequencing data generated in this study have been deposited in the GEO NCBI under the accession code GSE264654. All other data are available in the main text or supplementary materials. Source data are provided with this paper.

References

1. Montecino-Rodriguez, E. & Dorshkind, K. B-1 B cell development in the fetus and adult. *Immunity* **36**, 13–21 (2012).
2. Berland, R. & Wortis, H. H. Origins and functions of B-1 cells with notes on the role of CD5. *Annu. Rev. Immunol.* **20**, 253–300 (2002).
3. Nagasawa, T. Microenvironmental niches in the bone marrow required for B-cell development. *Nat. Rev. Immunol.* **6**, 107–116 (2006).
4. Pillai, S. & Cariappa, A. The follicular versus marginal zone B lymphocyte cell fate decision. *Nat. Rev. Immunol.* **9**, 767–777 (2009).
5. Cariappa, A. et al. The follicular versus marginal zone B lymphocyte cell fate decision is regulated by Aiolos, Btk, and CD21. *Immunity* **14**, 603–615 (2001).
6. Wen, L. et al. Evidence of marginal-zone B cell-positive selection in spleen. *Immunity* **23**, 297–308 (2005).
7. Rauch, M., Tussiwand, R., Bosco, N. & Rolink, A. G. Crucial role for BAFF-BAFF-R signaling in the survival and maintenance of mature B cells. *PLoS ONE* **4**, e5456 (2009).
8. Khan, W. N. B cell receptor and BAFF receptor signaling regulation of B cell homeostasis. *J. Immunol.* **183**, 3561–3567 (2009).
9. Saito, T. et al. Notch2 is preferentially expressed in mature B cells and indispensable for marginal zone B lineage development. *Immunity* **18**, 675–685 (2003).
10. Tanigaki, K. et al. Notch-RBP-J signaling is involved in cell fate determination of marginal zone B cells. *Nat. Immunol.* **3**, 443–450 (2002).
11. Garis, M. & Garrett-Sinha, L. A. Notch signaling in B cell immune responses. *Front. Immunol.* **11**, 609324 (2020).
12. Moriyama, Y. et al. Delta-like 1 is essential for the maintenance of marginal zone B cells in normal mice but not in autoimmune mice. *Int Immunol.* **20**, 763–773 (2008).
13. Bray, S. J. Notch signalling: a simple pathway becomes complex. *Nat. Rev. Mol. Cell Biol.* **7**, 678–689 (2006).
14. Gomez Atria, D. et al. Stromal Notch ligands foster lymphopenia-driven functional plasticity and homeostatic proliferation of naive B cells. *J. Clin. Investig.* **132**, e158885 (2022).
15. Hwang, I. Y., Boularan, C., Harrison, K. & Kehrl, J. H. Galpha(i) signaling promotes marginal zone B cell development by enabling transitional B cell ADAM10 expression. *Front. Immunol.* **9**, 687 (2018).
16. Cerutti, A., Cols, M. & Puga, I. Marginal zone B cells: virtues of innate-like antibody-producing lymphocytes. *Nat. Rev. Immunol.* **13**, 118–132 (2013).
17. Martin, F., Oliver, A. M. & Kearney, J. F. Marginal zone and B1 B cells unite in the early response against T-independent blood-borne particulate antigens. *Immunity* **14**, 617–629 (2001).
18. Klein, U. & Dalla-Favera, R. Germinal centres: role in B-cell physiology and malignancy. *Nat. Rev. Immunol.* **8**, 22–33 (2008).
19. Liu, X., Zhao, Y. & Qi, H. T-independent antigen induces humoral memory through germinal centers. *J. Exp. Med.* **219**, e20210527 (2022).
20. Cinamon, G., Zachariah, M. A., Lam, O. M., Foss, F. W. Jr & Cyster, J. G. Follicular shuttling of marginal zone B cells facilitates antigen transport. *Nat. Immunol.* **9**, 54–62 (2008).
21. Porsch, F., Mallat, Z. & Binder, C. J. Humoral immunity in atherosclerosis and myocardial infarction: from B cells to antibodies. *Cardiovasc Res* **117**, 2544–2562 (2021).
22. Honda, S. et al. Marginal zone B cells exacerbate endotoxic shock via interleukin-6 secretion induced by Fcalpha/muR-coupled TLR4 signalling. *Nat. Commun.* **7**, 11498 (2016).
23. Sakaguchi, T. et al. TRPM5 negatively regulates calcium-dependent responses in lipopolysaccharide-stimulated B lymphocytes. *Cell Rep.* **31**, 107755 (2020).
24. Liu, D. et al. IL-10-dependent crosstalk between murine marginal zone B cells, macrophages, and CD8alpha(+) dendritic cells promotes Listeria monocytogenes infection. *Immunity* **51**, 64–76.e67 (2019).
25. Liu, J. et al. Fcmicro receptor promotes the survival and activation of marginal zone B Cells and protects mice against bacterial sepsis. *Front. Immunol.* **9**, 160 (2018).
26. Lee, Y. Regulation and function of capicua in mammals. *Exp. Mol. Med.* **52**, 531–537 (2020).
27. Jimenez, G., Guichet, A., Ephrussi, A. & Casanova, J. Relief of gene repression by torso RTK signaling: role of capicua in Drosophila terminal and dorsoventral patterning. *Genes Dev.* **14**, 224–231 (2000).
28. Fores, M. et al. A new mode of DNA binding distinguishes Capicua from other HMG-box factors and explains its mutation patterns in cancer. *PLoS Genet.* **13**, e1006622 (2017).
29. Shin, D. H. & Hong, J. W. Capicua is involved in Dorsal-mediated repression of zerknullt expression in Drosophila embryo. *BMB Rep.* **47**, 518–523 (2014).
30. Lee, Y. et al. ATXN1 protein family and CIC regulate extracellular matrix remodeling and lung alveolarization. *Dev. Cell* **21**, 746–757 (2011).
31. Wong, D. et al. TRIM25 promotes Capicua degradation independently of ERK in the absence of ATXN1L. *BMC Biol.* **18**, 154 (2020).
32. Choi, N. et al. miR-93/miR-106b/miR-375-CIC-CRABP1: a novel regulatory axis in prostate cancer progression. *Oncotarget* **6**, 23533–23547 (2015).
33. Kim, E. et al. Capicua suppresses hepatocellular carcinoma progression by controlling the ETV4-MMP1 axis. *Hepatology* **67**, 2287–2301 (2018).
34. Kim, J. W., Ponce, R. K. & Okimoto, R. A. Capicua in human cancer. *Trends Cancer* **7**, 77–86 (2021).
35. Lee, J. S. et al. Capicua suppresses colorectal cancer progression via repression of ETV4 expression. *Cancer Cell Int.* **20**, 42 (2020).
36. Okimoto, R. A. et al. Inactivation of Capicua drives cancer metastasis. *Nat. Genet.* **49**, 87–96 (2017).
37. Yoe, J., Kim, D., Kim, S. & Lee, Y. Capicua restricts cancer stem cell-like properties in breast cancer cells. *Oncogene* **39**, 3489–3506 (2020).
38. Kim, S. et al. Regulation of positive and negative selection and TCR signaling during thymic T cell development by capicua. *Elife* **10**, e71769 (2021).
39. Park, G. Y. et al. Deletion timing of Cic alleles during hematopoiesis determines the degree of peripheral CD4(+) T cell activation and proliferation. *Immune Netw.* **20**, e43 (2020).
40. Park, S. et al. Capicua deficiency induces autoimmunity and promotes follicular helper T cell differentiation via derepression of ETV5. *Nat. Commun.* **8**, 16037 (2017).
41. Park, S., Park, J., Kim, E. & Lee, Y. The capicua/ETS translocation variant 5 axis regulates liver-resident memory CD8(+) T-cell

development and the pathogenesis of liver injury. *Hepatology* **70**, 358–371 (2019).
42. Park, J. et al. ETV5 promotes lupus pathogenesis and follicular helper T cell differentiation by inducing osteopontin expression. *Proc. Natl. Acad. Sci. USA* **121**, e2322009121 (2024).
43. Hong, H. et al. Postnatal regulation of B-1a cell development and survival by the CIC-PER2-BHLHE41 axis. *Cell Rep.* **38**, 110386 (2022).
44. Hong, H. & Lee, Y. Generation of hematopoietic lineage cell-specific chimeric mice using retrovirus-transduced fetal liver cells. *STAR Protoc.* **3**, 101526 (2022).
45. Kreslavsky, T. et al. Essential role for the transcription factor Bhlhe41 in regulating the development, self-renewal and BCR repertoire of B-1a cells. *Nat. Immunol.* **18**, 442–455 (2017).
46. Didonna, A. et al. Ataxin-1 regulates B cell function and the severity of autoimmune experimental encephalomyelitis. *Proc. Natl. Acad. Sci. USA* **117**, 23742–23750 (2020).
47. Cariappa, A. & Pillai, S. Antigen-dependent B-cell development. *Curr. Opin. Immunol.* **14**, 241–249 (2002).
48. Myers, D. R., Zikherman, J. & Roose, J. P. Tonic signals: why do lymphocytes bother? *Trends Immunol.* **38**, 844–857 (2017).
49. Garg, A. et al. FGF-induced Pea3 transcription factors program the genetic landscape for cell fate determination. *PLoS Genet.* **14**, e1007660 (2018).
50. Clementz, A. G., Rogowski, A., Pandya, K., Miele, L. & Osipo, C. NOTCH-1 and NOTCH-4 are novel gene targets of PEA3 in breast cancer: novel therapeutic implications. *Breast Cancer Res.* **13**, R63 (2011).
51. Boyle, P. & Despres, C. Dual-function transcription factors and their entourage: unique and unifying themes governing two pathogenesis-related genes. *Plant Signal. Behav.* **5**, 629–634 (2010).
52. McKenzie, G. et al. Cellular Notch responsiveness is defined by phosphoinositide 3-kinase-dependent signals. *BMC Cell Biol.* **7**, 10 (2006).
53. Villegas, S. N. et al. PI3K/Akt cooperates with oncogenic Notch by inducing nitric oxide-dependent inflammation. *Cell Rep.* **22**, 2541–2549 (2018).
54. Gutierrez, A. & Look, A. T. NOTCH and PI3K-AKT pathways intertwined. *Cancer Cell* **12**, 411–413 (2007).
55. Palomero, T. et al. Mutational loss of PTEN induces resistance to NOTCH1 inhibition in T-cell leukemia. *Nat. Med.* **13**, 1203–1210 (2007).
56. Meurette, O. et al. Notch activation induces Akt signaling via an autocrine loop to prevent apoptosis in breast epithelial cells. *Cancer Res.* **69**, 5015–5022 (2009).
57. Tong, X. et al. Ataxin-1 and Brother of ataxin-1 are components of the Notch signalling pathway. *EMBO Rep.* **12**, 428–435 (2011).
58. Lu, H. C. et al. Disruption of the ATXN1-CIC complex causes a spectrum of neurobehavioral phenotypes in mice and humans. *Nat. Genet.* **49**, 527–536 (2017).
59. de Boer, J. et al. Transgenic mice with hematopoietic and lymphoid specific expression of Cre. *Eur. J. Immunol.* **33**, 314–325 (2003).
60. Rickert, R. C., Roes, J. & Rajewsky, K. B lymphocyte-specific, Cre-mediated mutagenesis in mice. *Nucleic Acids Res.* **25**, 1317–1318 (1997).
61. Matilla, A. et al. Mice lacking ataxin-1 display learning deficits and decreased hippocampal paired-pulse facilitation. *J. Neurosci.* **18**, 5508–5516 (1998).
62. Bowman, A. B. et al. Duplication of Atxn1l suppresses SCA1 neuropathology by decreasing incorporation of polyglutamine-expanded ataxin-1 into native complexes. *Nat. Genet.* **39**, 373–379 (2007).
63. Song, Y. & Lee, Y. Brief guide to flow cytometry. *Mol. Cells* **47**, 100129 (2024).
64. Mikami, M. et al. RUNX1-Survivin Axis Is a Novel Therapeutic Target for Malignant Rhabdoid Tumors. *Mol. Cells* **45**, 886–895 (2022).
65. Kim, J. A. et al. Temporal transcriptome analysis of SARS-CoV-2-infected lung and spleen in human ACE2-transgenic mice. *Mol. Cells* **45**, 896–910 (2022).
66. Kim, E. et al. Deficiency of Capicua disrupts bile acid homeostasis. *Sci. Rep.* **5**, 8272 (2015).

Acknowledgements

We thank the members of Lee laboratory for their inputs and comments on the study, and Dr. Huda Y. Zoghbi for kindly providing *Atxn1*$^{-/-}$, *Atxn1l* floxed, and *Cic* floxed mice. This study was supported by the National Research Foundation (NRF) of Korea grants funded by the Korean government (2021R1A6A1A10042944, 2022M3E5F2018020, RS-2023-00260454, and RS-2024-00336114), the Korea Basic Science Institute (National Research Facilities and Equipment Center) grant funded by the Ministry of Education (2021R1A6C101A390), and the BK21 FOUR grant funded by the Ministry of Education, Republic of Korea. (4120240315124). J.L. was supported by a Global PhD Fellowship (NRF-2018H1A2A1059794). Y.H. was supported by the Basic Science Research Program of the NRF of Korea funded by the Ministry of Education (RS-2023-00276340).

Author contributions

Conceptualization: J.S.P., H.H., and Y.L.; Methodology: J.S.P., H.B.K., T.K.K., and Y.L.; Investigation: J.S.P., M.K., H.H., J.L., Y.S., Y.H., and S.K.; Writing—original draft: J.S.P. and Y.L.; Writing—review & editing: T.K.K. and Y.L.; Visualization: J.S.P. and Y.L.; Supervision: Y.L.; Funding acquisition: Y.L.

Competing interests

The authors declare no competing interests.

Additional information

Supplementary information The online version contains supplementary material available at https://doi.org/10.1038/s41467-024-54803-z.

Correspondence and requests for materials should be addressed to Yoontae Lee.

Peer review information *Nature Communications* thanks Stephen Yip and the other, anonymous, reviewer(s) for their contribution to the peer review of this work. A peer review file is available.